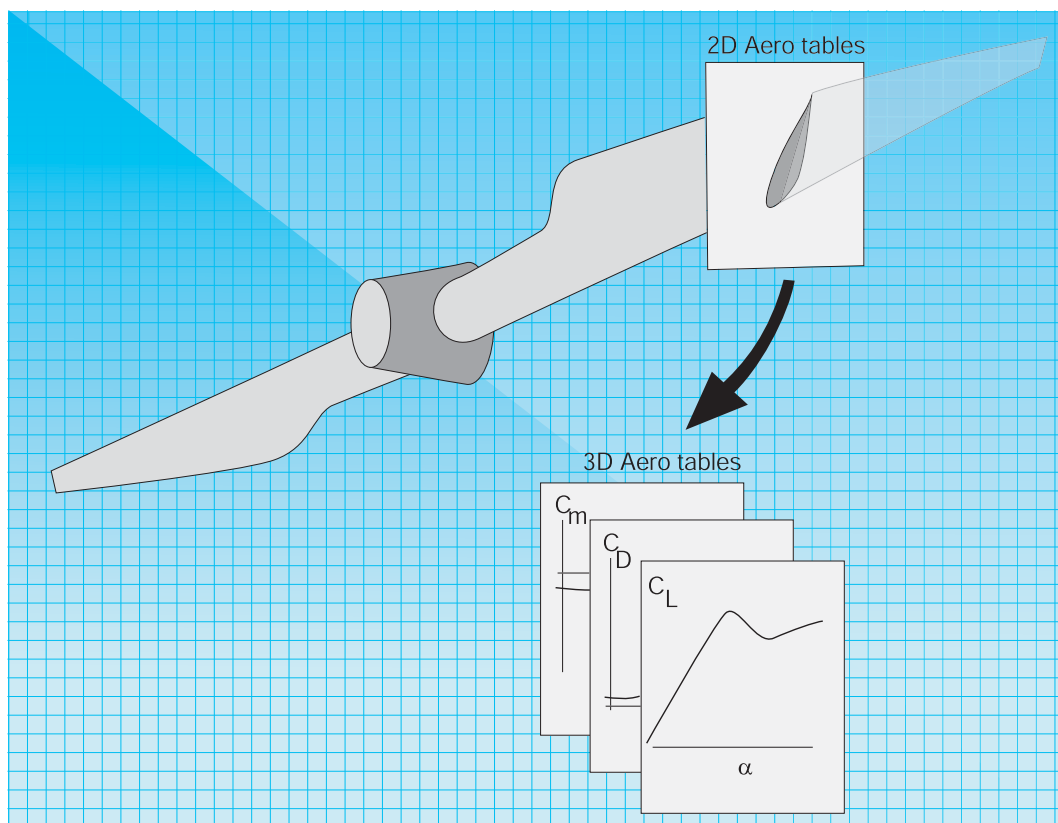


Björn Montgomerie

# Methods for Root Effects, Tip Effects and Extending the Angle of Attack Range to $\pm 180^\circ$ , with Application to Aerodynamics for Blades on Wind Turbines and Propellers





SWEDISH DEFENCE RESEARCH AGENCY

Aeronautics, FFA  
SE-172 90 Stockholm

FOI-R--1305--SE

June 2004

ISSN 1650-1942

**Scientific  
report**

Björn Montgomerie

**Methods for Root Effects, Tip Effects and  
Extending the Angle of Attack Range to  $\pm 180^\circ$ , with  
Application to Aerodynamics for Blades on Wind  
Turbines and Propellers**



# CONTENTS

NOTATION .....	6
1. INTRODUCTION .....	9
2. EXTENDING AERODYNAMIC CURVES FOR LIFT, DRAG AND MOMENT TO $\pm 180^\circ$ ANGLE OF ATTACK.....	11
2.2 LIFT COEFFICIENT - CL .....	11
2.2.1 Extending the Alpha Range .....	11
2.2.2 The transformation function f .....	12
2.2.3 The Potential Flow Lift Function t .....	14
2.2.4 Fully Separated Flow on Cambered Thin Plates – Function s .....	14
2.3 DRAG COEFFICIENT - CD.....	17
2.3.1 Finding CD90 .....	17
2.3.2 Using CD90 to Create CD .....	19
2.4 MOMENT COEFFICIENT - CM .....	20
2.4.1 Aerodynamic Centers .....	20
2.4.2 Moment Arm and its Relation to CL and CD .....	21
2.4.3 Summary of the Cm Calculation Technique .....	27
3. END EFFECTS .....	29
3.1 OVERVIEW OF END EFFECTS .....	29
3.2 GRADIENT EFFECTS .....	29
3.2.1 Tip Effects – Attached Flow .....	30
3.2.2 Tip Effects – Detached Flow .....	38
3.3 THE HIMMELSKAMP EFFECT .....	35
3.3.1 CL Modification .....	35
3.3.2 CD Modification .....	38
3.3.3 Cm Modification .....	40
3.3.4 Variability with RPM .....	42
3.3.5 Summary of Measures taken to Account for the Himmelskamp Effect .....	42
4. TOPICS FOR FUTURE INVESTIGATION .....	43
5. REFERENCES .....	45
Appendix A -NORMAL COEFFICIENT AS A FUNCTION OF ANGLE OF ATTACK AND SEPARATION LOCATION .....	49

## NOTATION

### Latin:

- $a$  = Lift coefficient increment as defined in Fig. 1  
 $A$  = Amplitude manipulation factor in thin plate artificial lift generation, see Eq. (19)  
 $a$  = CL curve elevation caused by the Himmelskamp effect, see Fig. 31 and  $\delta CL$   
 $a$  = CL difference between potential flow line and 2D curve, see Fig. 18  
 $A$  = Point in  $C_L$  vs  $\alpha$  according to Fig. 1  
 $A'$  = Point in  $C_L$  vs  $\alpha$  according to Fig. 1  
 $A$  = Blade tip area as defined in Fig. 27  
 $A_M$  = Point in CL vs  $\alpha$  according to Fig. 1  
 $\alpha_{min}$  = Angle of attack value where CL is minimum, see Eq. (3)  
 $arm$  = Moment arm counted from the leading edge of the wing profile  
 $arm0$  = Moment arm length at around  $\alpha = 0$ , see Sect. 2.4.2  
 $armCalc$  = Simplified estimate of the moment arm defined in Sect. 2.4.2  
 $armLine$  = Linear approximation for the moment arm in the deep stall positive  $\alpha$  region, see Eq. (45)  
 $armNeg$  = Linear moment arm approximation for negative  $\alpha$ , see Sect. 2.4.2  
 $b$  = CL difference between 2D curve and thin plate CL deep stall curve, see Fig. 18  
 $b$  = CL difference between potential flow line and 2D curve, see Fig. 31  
 $b$  = Effective span measure as defined in Fig. 9  
 $b$  = Lift coefficient increment as defined in Fig. 1  
 $B$  = Point in CL vs  $a$  according to Fig. 1  
 $B_M$  = Point in CL vs  $a$  according to Fig. 1  
 $c$  = Chord length  
 $C_D$  = General drag coefficient  
 $C_{D,thinPlate}$  = CD value for a thin (possibly cambered) plate with fully separated flow  
 $C_{D2D}$  = CD data valid for 2D flow  
 $C_{D3D}$  = CD data valid for 3D flow, possibly including effects in the boundary layer from rotation  
 $C_{D90}$  = Drag coefficient at 90 deg angle of attack  
 $C_L$  = Lift coefficient  
 $C_{L,max}$  = Maximum CL at typically 16 deg  
 $C_{L,min}$  = Minimum CL at typically -14 deg  
 $CL_{thinPlate}$  = CL value for a thin (possibly cambered) plate with fully separated flow  
 $C_{L0}$  = Lift coefficient caused by profile camber, see e.g. Fig. 15  
 $C_{L2D}$  = CL for two-dimensional flows  
 $C_{L90}$  = Lift coefficient at 90 deg angle of attack  
 $C_{L\alpha}$  = Lift coefficient slope with  $\alpha$   
 $C_m$  = Wing profile moment coefficient  
 $C_N = C_n$  = Normal coefficient  
 $e$  = Exponent in expression (69)  
 $f$  = Interpolation function for moment arm calculation, see Eqs. (43) and (44)  
 $f$  = Kirchoff proportion of profile suction side having attached flow - ( $0 < f < 1.0$ )  
 $f$  = Transition function for  $C_L$  interpolation, see definition in Eq. (5) and Fig. 3  
 $g$  = Reduction factor on 2D coefficient to yield a 3D ditto, see Eq. (69)  
 $h$  = 360 degree range interpolation function according to Eq. (76)  
 $h$  = Camber line maximum height, see Sect. 3.3.5  
 $h$  = Lift increment defined in Fig. 2  
 $h1, h2, h3$  and  $h4$  = Components of  $h$  according to Eq. (76)  
 $k$  = Coefficient defined in Eq. (1)  
 $k$  = Factor defined in Eq. (74)  
 $k^*$  = Coefficient defined in Eq. (1)  
LAR = Local area aspect ratio, see Sect. 3.2  
 $offset$  = Component in the estimate of  $armLine$ , see Eq. (46)

$p$  = Factor of proportionality to apply in the separation of Himmelskamp lift effects, see Eq. (82) and (84)  
 $r$  = Blade radial coordinate  
 $rawSnelCL$  = same as the basic Snel expression as applied near 0 and near 180 deg, see Eq. (77)  
 $r_{LE}$  = Wing profile leading edge radius  
 $s$  = Thin plate lift function value seen in Fig. 2  
 $slope$  = Component in the estimate of  $armLine$ , see Eq. (47)  
 $t$  = Potential flow idealized lift line as defined in Fig. 2  
 $t$  = Wing profile thickness  
 $y$  = Coordinate counted from the blade tip and inward, see Fig. 27

**Greek:**

$\alpha$  = Angle of attack  
 $\alpha^*$  = Angle of attack shift defined in Eq. (75)  
 $\alpha_0$  = Angle of attack where  $CL = 0$   
 $\alpha_1$  = Arbitrary point chosen according to instruction near Eq. (7)  
 $\alpha_2$  = Arbitrary point chosen according to instruction near Eq. (7)  
 $\alpha_M$  = Point of departure from potential flow to fully separated, see Fig. 2  
 $\beta$  = Rear flank wing profile angle, see Fig. 35  
 $\beta$  = Thin plate lift modification angle according to Eq. (14)  
 $\delta 1$  = Thin plate manipulation angle according to Eqs. (14), (15) and (16)  
 $\delta 2$  = Thin plate manipulation angle according to Eqs. (14), (15) and (16)  
 $\Delta\alpha_{min}$  = Parameter defined in Eq. (3)  
 $\delta C_L$  =  $C_L$  curve elevation caused by the Himmelskamp effect, see Eqs. (73) and (89)  
 $\Delta C_L$  =  $C_L$  increment at 25% chord caused by angle of attack, See Fig. 15  
 $\Delta C_L$  = Difference between  $CL$  for potential flow line and  $CL_{2D}$ , see Fig. 11  
 $\Delta C_{L,circ}$  =  $CL$  increment defined in Fig. 36  
 $\Delta C_{L,vort}$  =  $CL$  increment defined in Fig. 36  
 $\kappa$  = Factor on chord as defined in Eqs. (27)  
 $\lambda$  = Local speed ratio as defined in Sect. 3.3.4





# 1. INTRODUCTION

Two areas of practical importance for implementing wind turbine and propeller aerodynamic computer code are addressed in this report. The text deals partly with modifications to the two-dimensional aerodynamic coefficient functions and partly with methods for extending the angle of attack interval. One fundamental assumption is that steady state aerodynamic tables can be used together with unsteady aerodynamics. The latter effects are then added to the steady state values. This report deals only with the steady part.

Aerodynamic information usually comes in a package containing lift, drag and moment vs angle of attack. But, the information is valid only for a range that is of interest for airplane analysis, a context where deep stall is of minor interest because it was always avoided. In wind turbine technology deep stall is sometimes invited in high winds as the means to limit excessive power, usually without pitching the blades.

Analysis of tests, coming from the early stall controlled wind turbines (~1980), revealed considerable deviation from what had been predicted when the turbines were designed. The prominent difference consisted in a discrepancy in torque. The real turbine performed much “better” than predicted once the stall region was experienced. This typically occurred at a wind velocity of about 12 m/s and up.

The matter was investigated and a three-dimensional aerodynamic effect, associated with the centrifugal loading of the blade boundary layer, not accounted for in the analysis at the time, was identified as the main cause for the large discrepancy in torque. Numbers of 10 to 25 % of difference between prediction and measurement were recorded. Reports generated by German researcher Himmelskamp at around 1940 came under scrutiny. He performed wind tunnel tests on instrumented propellers, allowing the evaluation of pressure distributions, and he presented lift coefficient ( $C_L$ ) values in excess of 3.0 for radial stations near the hub. Although Himmelskamp found the consequences of this particular aerodynamic phenomenon he did not present a theory explaining his findings.

Qualitative explanations of the Himmelskamp effect were presented in the late 80s. Notably Dutch researcher H. Snel et al derived a simplified set of two-dimensional Navier – Stokes boundary layer equations, where centrifugal and consequential Coriolis effects were accounted for. It appears, in their final corrective expression for  $C_L$ , that the crucial factor, driving the Himmelskamp effect, is chord divided by radius ( $c/r$ ). This method was expedient to use as an add-on to existing code. The correction term, originally containing two constants, is now being widely used in the wind turbine industry with various adaptations of the constants to measured data. This is of equal interest in fixed pitch propeller analysis, particularly at takeoff conditions. The Snel approach is applied also in this report with some additional thoughts for the corresponding profile drag and moment effects.

Further modification to two-dimensional data are effects associated with radial pressure gradients near the tip. These have been observed to have a lowering effect on both lift curve slope and  $C_L$  maximum.

The present main trend in manufacturing is seen to favor pitch control, which is used to avoid separated flow over the blade surface. The influence of the Himmelskamp effect is then negligible in normal operating conditions. However, pitch control is also used in some designs to control stall. In this case stall is intentionally invited as the means to reduce the loading when the wind increases over rated wind speed. The fixed pitch, stall controlled turbines, which were omnipotent in the eighties, are becoming more rare. But, their continued existence, and the fact that all turbines can have control errors requires the calculation of loads from separated flow on the blades in order to account for normal operational as well as extreme load cases.

The other area addressed in this report is the extension of the aerodynamic tables to be valid in the full 360 degrees interval of angle of attack. This need comes from practical application of aerodynamic code inside of aeroelastic programs. The latter are frequently used to investigate the elastic behavior of the whole wind turbine in response to gravity loading and variable wind conditions. In a start-up sequence the wind

turbine may be directed out of the wind such that the slowly turning blade is chased by the wind from behind. This may cause angles of attack that are near 180 degrees. In order not to extrapolate the aerodynamic tables, from typically available 20 degrees, an approximate representation for the full 360 degree interval is necessary.

Also of interest, at high angles of attack, are the plus and minus 90 degrees angle of attack vicinities. These have relevance for self starting torque especially if the blades are fixed as is frequently the case in stall controlled turbines.

The general approach to reach the described accomplishments is to apply curve fit generalizations to measured data. The background material varies from being dependable down to outright guesswork. Fortunately, in the latter case, the importance of accuracy is little, e.g. the aerodynamics around 180 degrees of angle of attack.

The curve fits mostly include model parameters that can be changed as new data from measurement, and hopefully CFD, become available. The total methodology therefore includes a number of such parameter to be monitored by any user. But, this document recommends default values which are judged to be a present "best guess". The typical need for modifying these parameters occurs in the context of applying the described methods in computer programs aiming at the prediction of loads and performance for wind turbine rotors and propellers.

Although the author of this text is active in the wind turbine aerodynamics area and the text therefore is slanted toward turbines, there is no basic difference between the aerodynamics for turbine and propeller. In practical application, however, the propeller analyst will find some extensions, of the aerodynamic tables to numerically very large negative values, to be of little interest. In this light turbine aerodynamics can be seen as encompassing and exceeding the propeller aerodynamic needs.

## 2. EXTENDING AERODYNAMIC CURVES FOR LIFT, DRAG AND MOMENT TO $\pm 180^\circ$ ANGLE OF ATTACK

### 2.1 THE NEED FOR THE $\pm 180^\circ$ ANGLE OF ATTACK INTERVAL

Usually the aerodynamic curves of  $C_L$ ,  $C_D$  and  $C_m$  vs angle of attack are presented in an angular interval extending from say  $-5$  to  $+20$  degrees. In wind turbine performance simulation, there is a need to extend the normally available aero tables to the full 360 degree range. For this purpose thin plate theory (complete stall) complemented with the linear range behavior (potential flow model) is used. The following text treats  $C_L$ ,  $C_D$  and  $C_m$  in separate sections. It is assumed that a normal range angle of attack set of curves is the raw material from which data are extended.

### 2.2 LIFT COEFFICIENT - $C_L$

#### 2.2.1 Extending the Alpha Range

The basic thin plate curve, see Sect. 2.2.4, is used as a base, which the extended curve will approach asymptotically. However, in the  $-15$  to  $+15$  degree region and also around  $180^\circ$  there will be some potential-flow-like behavior of a real case, which should be emulated.

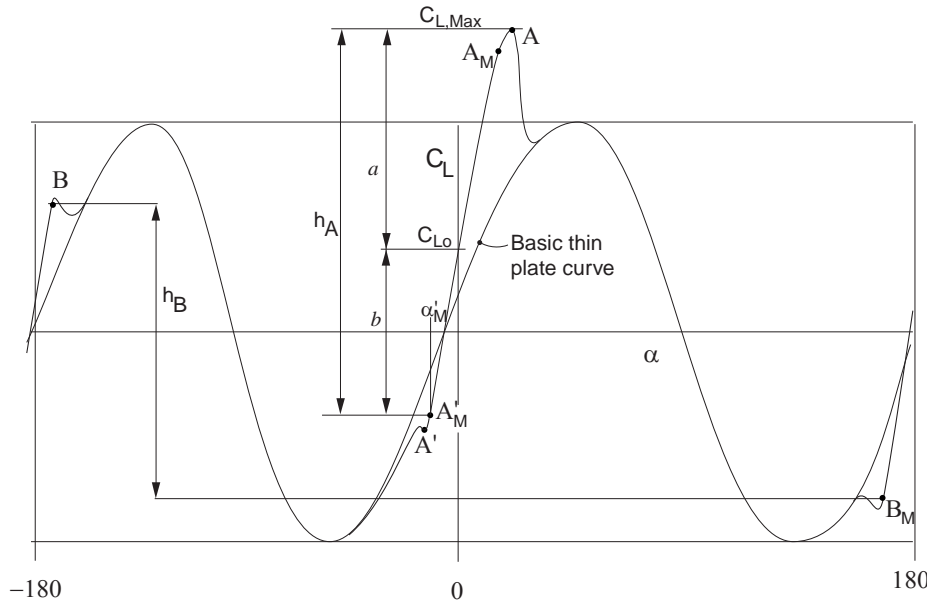


Figure 1

The complete top region of A is usually known whereas its lowest part, around A', corresponding to  $C_{L,min}$ , is frequently not available. The theory to find the lower apex (lower end of the  $h_A$  measure arrow) will emerge from the idea that  $h_A$  depends on  $C_{L,max}$  and camber. The case without camber can serve as a starting point for this discourse. Because of geometrical symmetry there will also be a symmetry in the  $C_L$  curve such that  $C_{L,min} = -C_{L,max}$ . With a cambered airfoil, which is created to operate in a positive angle of attack range, the performance on the negative side will be relatively poor. This means that the cambered airfoil does not simply move the  $C_L$  curve up as a rigid object. Therefore,  $b \neq a$ . The ratio  $b/a$  should therefore change as  $C_L(0)$  increases. The following expression of proportionality is proposed for  $b$ .

$$b = k \cdot a \equiv \{1 - k^* \cdot C_L(0)\} \cdot \{C_{L,max} - C_L(0)\} \quad (1)$$

where  $k^*$  is a model parameter which should depend on Reynolds number, nose radius and camber shape. But, no such connection is known to the author. A value of  $k^* = 0$  is tentatively proposed. From Fig. 1:

$$C_{L,min} = C_L(0) - b \quad (2)$$

This relation can perhaps be accepted on the grounds that hitting the minimum is usually not of extreme importance. The expression for  $k$  could easily be modified to reflect any measurements of other behavior than linear, should such data become available in the future.

Point A' is further defined by an angle of attack value. It should be slightly smaller, i.e. more to the left, than the potential flow straight line would indicate, see Fig. 2. The following expression arises from this idea.

$$\alpha_{\min} = \frac{C_{L,\min} - C_L(0)}{2\pi} - \Delta\alpha_{\min} \quad (3)$$

where  $\Delta\alpha_{\min}$  is typically say +3 degrees. However, the point A'=(amin,CLmin) will be used for *reference* only. This will become clear in Sect. 2.2.2.

### 2.2.2 The transformation function $f$

The shape of the  $C_L$  curve, left of A'\_M and right of A\_M, will be constructed using a certain function  $f$ . This function, which can be seen as a transformation of  $C_L$ , is used for interpolation between the curves for attached flow (t) and fully separated flow (s) to yield the  $C_L$  curve. Explanation and definition of  $f$  follows.

When an airfoil undergoes an increase from zero degrees angle of attack ( $\alpha$ ) to say 50 degrees, the following happens. First the flow behaves very much like potential flow, i.e. the lift curve slope vs  $\alpha$  is near  $2\pi$  and drag is minimal. In this situation  $f = 1.0$ . At 50 degrees the flow on the suction side of the airfoil is separated and this very non-potential flow produces a substantial drag force. In this situation  $f = 0$  and the wing behaves very much like a thin plate with a sharp leading edge.

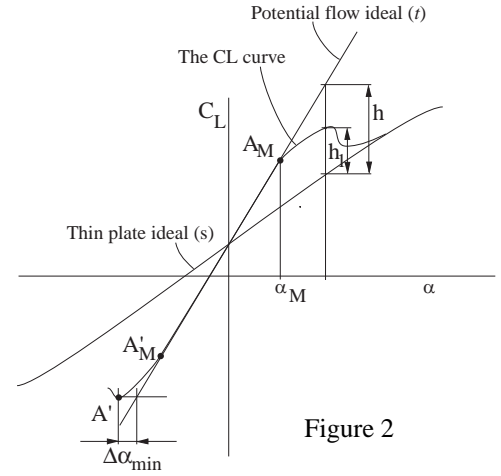


Figure 2

Between the two described situations a transition, from potential flow ( $t$ ) to fully separated flow ( $s \equiv C_{L,thinPlate}$ ), takes place, see Fig. 2, “the CL curve”. This transition can be thought of as an interpolation between  $t$  and  $s$ . The function  $f$  decreases from its value 1.0, around zero angle of attack, to zero for high (or very small i.e. negative) alphas. In this model the  $f$  curve leaves  $t$  at some “anchor” point A\_M where  $\alpha = \alpha_M$ . Angles of attack are then used to create the differential angle  $\Delta\alpha$  where

$$\Delta\alpha = \alpha_M - \alpha \quad (4)$$

Glancing in advance at Eq. (6), which is symmetrical, it will turn out that this definition is valid for the negative side and the positive side alike. The *definition* of  $f$  is

$$f \equiv \frac{h_1}{h} \left( = \frac{C_L - s}{t - s} \right) \quad (5)$$

So, if all three curves ( $C_L$ ,  $s$  and  $t$ ) are known beforehand, it is a simple matter to calculate  $f$ . After studying a few airfoil  $C_L$  curves and after numerical manipulations using Excel the following *curve fit* expression for  $f$  was arrived at. It is proposed as a substitute for more rigorous data mining of general  $C_L$  behaviors.

$$f = \frac{1}{1 + k \cdot \Delta\alpha^4} \quad (6)$$

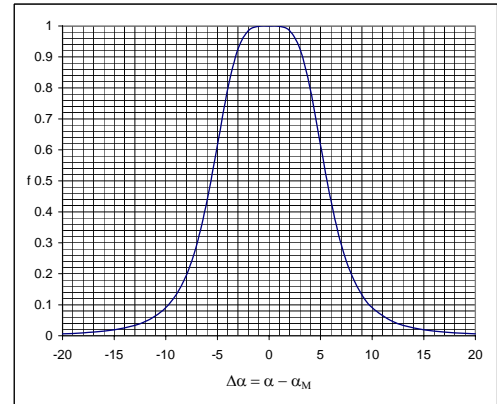


Figure 3

An example of the function  $f$ , for  $k=0.001$  is seen in Fig. 3. The negative side, of the bell shaped curve, reflects the  $C_L$  behavior on the negative side left of  $\alpha_M'$  in the  $C_L$  vs  $\alpha$  plane. The right side reflects the right  $C_L$  side at  $\alpha_M$  respectively. See Fig. 2 for notations.

Once the curve fit expression for  $f$  has been found, it can be applied for interpolation purposes as described above and by Eq. (10).

Obviously the expression for  $f$ , according to Eq. (6), contains two initially unknown constants  $k$  and  $\alpha_M$ . Using two points, from the given  $C_L$  vs  $\alpha$  curve, these constants can be solved for. This is typically always applied to the positive side of the curve. The last given point, on the original source curve, should be used as point 1. The second point (point 2) is taken from somewhere near the middle between where the  $C_L$  curve leaves  $t$  and the last given point. Applying Eq. (5) for two points in the  $(\alpha, f)$  plane two values of  $f$  are calculated. They are  $f_1$  and  $f_2$ . Using the two points, inserting in (6) and (5) and applying some algebra the following solution can be arrived at.

$$\alpha_M = \frac{\alpha_1 - G\alpha_2}{1 - G} \quad (7)$$

where

$$G \equiv \sqrt[4]{\frac{\frac{1}{f_1} - 1}{\frac{1}{f_2} - 1}} \quad (\text{Definition}) \quad (8)$$

and

$$k = \left( \frac{1}{f_2} - 1 \right) \frac{1}{(\alpha_2 - \alpha_M)^4} \quad (9)$$

Inserting the values for  $\alpha_M$  and  $k$  in Eq. (4) and (6) values of  $f$  can be calculated for any given value of  $\alpha$ . This is typically carried out for a series of  $\alpha$  values. Then the corresponding series of  $f$  values is converted to  $C_L$  values using

$$C_L = f \cdot t + (1 - f)s \quad (10)$$

where  $t$  is the straight line function being a tangent to the  $C_L$  curve at  $(\alpha=0, C_L=C_L(0))$ . Since  $0 < f < 1$  Eq. (10) gives a smooth interpolated transition from curve ( $t$ ) to  $s (= C_{L,thinPlate})$ , see definitions in Fig. 2.

If the negative value corresponding to  $C_{L,max}$ , i.e.  $C_{L,min}$ , is not present in the original data, it must be constructed as described above. Then Eqs. (7) through (10) are applied to the negative side as well.

It should be pointed out finally that creating an  $f$  function that gives back a  $C_{L,max}$  value at the right point, at the same time making it a maximum, is not a straight-forward matter. If the  $C_{L,max}$  point is known a numerical iteration must be applied in order to arrive at correct values of  $\alpha_M$ . Although it is true that Eqs. (7) through (9) could be evaluated letting one point e.g.  $(\alpha_1, C_{L1})$  be the maximum point on the  $C_L$  curve, the  $f$  curve created this way would give back the coordinate point for maximum. But, that point would not necessarily be a maximum! The whole matter boils down to the impossibility of having two points and one optimum to be satisfied while the curve fit expression only has two parameters (knobs) to set. I.e. three conditions cannot be satisfied with two equations only.

As explained the method requires that two points on the  $C_L$  curve be given in the transition between the "potential flow" curve and the thin plate separated flow curve. These points give some freedom to shape the curve. But, mostly these points are unknown. Mostly, however, a notion of the  $C_{L,max}$  level is present in the mind of the analyst. Therefore, there is a need for a practical selection procedure including  $C_{L,max}$  and

some elements of default. The idea is that  $C_{Lmax}$  and the default values should be used as an input to the procedure which outputs the two points on the transition curve. The following algorithm contains these ideas. Note that the positive side analysis is usually not necessary to carry out. It is already in basic data.

Algorithm positive side

1.  $\alpha_1 = \frac{C_{Lmax} - C_L(0)}{C_{L\alpha}} + \Delta\alpha_{min}$
2.  $C_{L1} = C_{Lmax}$
3.  $\alpha_2 = \alpha_1 + 15^\circ$
4.  $C_{L2} = s(\alpha_2) + 0.03$

Algorithm negative side

1.  $\alpha_1 = \frac{C_{Lmin} - C_L(0)}{C_{L\alpha}} - \Delta\alpha_{min}$
2.  $C_{L1} = C_{Lmin}$
3.  $\alpha_2 = \alpha_1 - 15^\circ$
4.  $C_{L2} = s(\alpha_2) - 0.03$

For the function  $s$ , see Sect. 2.2.4 below.

### 2.2.3 The Potential Flow Lift function $t$

The attached flow function  $t$  will be assumed to be a straight line obtained from the following expression.

$$t \equiv C_{L,attach} = C_L(0) + C_{L\alpha} \alpha \quad (11)$$

where the slope  $C_{L\alpha}$  is obtained from points near  $\alpha = 0$  on the given basic  $C_L$  curve if the curve can be seen as two-dimensional.

$$C_{L\alpha} = \text{Slope of given input curve} \quad (12)$$

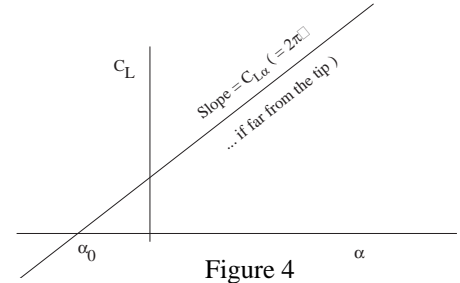


Figure 4

### 2.2.4 Fully separated Flow on Cambered Thin Plates – Function $s$

Two important effects from real wings modify the basic flat plate curve. These real effects are camber and rounded nose. Camber gives rise to a positive  $C_L$  value at an angle of attack ( $\alpha$ ) that equals 0. The rounded nose, on the real airfoil, causes a modest positive lift coefficient at positive angles of attack. At 90 degrees it is typically 0.08 according to Ref. 1. Ref. 1 is one prominent exception to the rule that data are only available in a limited angle of attack range. It can therefore serve as a reference for a curve that is a blend between an airfoil and a flat plate. Ref. 1 describes the wind tunnel testing of a wing with the NACA 0012 profile at all angles of attack.

The part of the aerodynamic curves for any given set of data must now be blended and slide over into the thin plate curve as the angle of attack gets larger or smaller toward the negative side. To accomplish a gentle blending, of the known values into the real curve, the following method using curve fit is proposed.

The technique is to initially only modify the angle of attack slightly. The original expression from Hoerner, Ref. 2, reads

$$C_{LflatPlateBasic} = CD_{90} \sin \alpha \cos \alpha \quad (13)$$

But, to modify for the real effects,  $\alpha$  is replaced by  $\beta$  whose definition is:

$$\beta = \alpha - \delta_1 - \delta_2 \quad (14)$$

where

$$\delta_1 = 57.6 \cdot C_{L90} \sin \alpha \dots \text{rounded nose effect, deg.} \quad (15)$$

$$\delta_2 = \alpha_0 \cos \alpha \dots \text{camber effect} \quad (16)$$

where

$\alpha_0$  = Zero lift angle of attack, degrees, usually a negative number.

$C_{L90}$  =  $C_L$  value desired at  $\alpha = 90^\circ$ , typically + 0.08.

The curves resulting from (12) and then (12), with  $\beta$  in place of  $\alpha$ , appear in Fig. 5. ( $CD_{90}=2.0$ )

The correction functions are seen in Fig. 6. In both figures the following numerical values were used.

$$C_{L90} = .08 \quad (17)$$

$$\alpha_0 = -4 \text{ deg.} \quad (18)$$

In the application of the formulae, it is important to use the zero lift angle of attack from the profile aerodynamic data graph or table, and use it also for the flat plate equations. Lift at 90 degrees may not always be known. The value used above may then be used as an approximation.

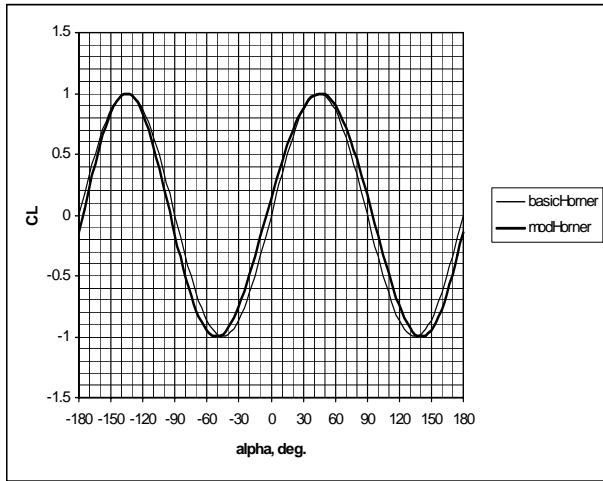


Figure 5

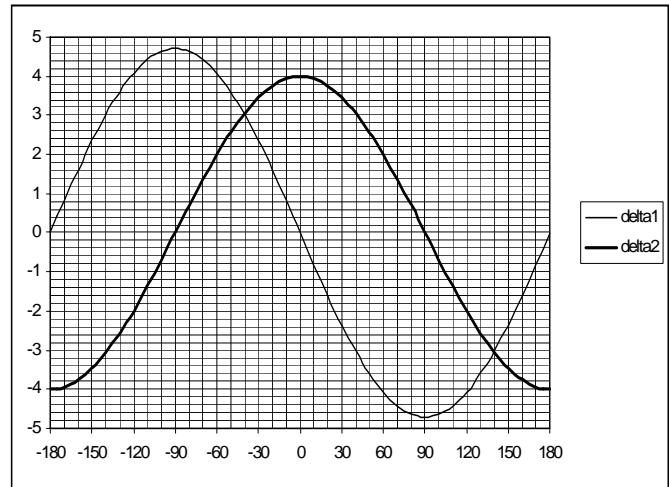


Figure 6

Another effect need also be modeled. Even a thin plate that is cambered will have an asymmetrical lift curve meaning that, its maximum positive value is higher than the absolute of the corresponding minimum value (at around  $-45 \text{ deg.}$ ). The simple form of the lift curve, according to Fig. 5, can be modified using a multiplier on the amplitude. That multiplier can be constructed to be  $1.0 +$  some relatively small variation with desired characteristics. The amplitude of this correction depends on camber. A measure of camber is the zero lift angle. Therefore, the zero lift angle is used to represent this effect.

Very little guidance can be had from the literature. This calls for some inventive approach. The idea applied here is to say that the elevation, of the sinusoidal curve at  $+45^\circ$  angle of attack, is the same as that at zero degrees. This leads to a multiplier function accordingly:

$$A = 1 + \frac{C_L(0)}{\sin 45^\circ} \sin \alpha \quad (19)$$

Summing up the complete method in an algorithm gives the following.

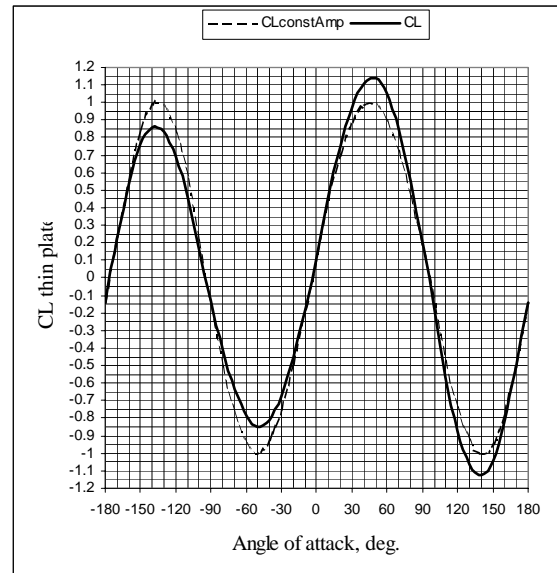


Figure 7

$$\delta_1 = 57.6 \cdot C_{L90} \sin \alpha \dots \text{rounded nose effect, deg.} \quad (20)$$

$$\delta_2 = \alpha_0 \cos \alpha \dots \text{camber effect} \quad (21)$$

$$\beta = \alpha - \delta_1 - \delta_2 \quad (22)$$

$$A = 1 + \frac{C_L(0)}{\sin 45^\circ} \sin \alpha \quad (23)$$

$$CL_{\text{curvedPlateBasic}} = A \cdot CD_{90} \sin \beta \cos \beta \quad (24)$$

The final curve, for  $\alpha_0 = -4$  deg.,  $C_{D90}=2$  and  $C_{L90}=.08$ , is seen in Fig. 7 together with the simpler approximation, the latter having constant amplitude.

### 180° Algorithm

The “rear-end-first-flying” also requires some crude estimate of the “linear” range of the curve.

Accuracy is probably not the concern in the 180 degrees area. It will be assumed that  $C_{Lmax}$  and  $C_{Lmin}$  corresponding to points B and A in Fig. 8, are symmetrically placed around the thin plate value at 180 degrees. The size remains to be estimated. One source of information comes from Critzos 1955 report, see Ref. 1. In the report the symmetrical NACA 0012 profile is investigated. At around 170° angle of attack the maximum (minimum)  $\Delta C_{L,180}$  is about -1.3 for smooth surface at  $Re = 1.8$  million.

At  $Re = 0.5$  million  $\Delta C_{L,180} = -.75$ . The latter number is confirmed by the Chinese measurements, see Ref. [12]. However, the Chinese measurements show that  $\Delta C_{L,180} = -.8$  for the Clark-Y airfoil while the FX72-MS-150A has a value of -1.0, valid also for the NACA64(2)-415. The value -.8 and -.7 are also recorded for the NACA4418 and 64(1)412 profiles respectively. All the Chinese measurements

were carried out at a  $Re$  of approximately ½ million. In summary no clear indicator exists what number to apply. There is only the knowledge that the numerical size varies between .7 and 1.0 and that the trend is increasing for increasing  $Re$ . It is known from Hoerner[2] that the normal (i.e. leading edge first) trend is not linear. Instead there is a precipitous rise in  $CL_{max}$  when  $Re$  goes from say 200000 to 300000. Then there appears to be a plateau up to one million followed by a gentle rise for still higher  $Re$  numbers. But, the trends referred to are valid for the leading-edge-first situation as mentioned. It is uncertain to draw firm conclusions for the trailing-edge-first from this material although it is the only material available at the time of writing. An attempt, to sketch the dependence on  $Re$ , is nevertheless presented in the summary below, see point a.

The slope can be assumed to be the same as for the near-zero region. With this simple basis a linear lift model can be established for the near 180° region as follows.

The  $\alpha$  range in the immediate 180° vicinity need be modeled with its linear characteristics. The data construction hinges upon a few assumptions. They are:

- a. A dependence on Reynolds number can be used as follows.

$$\Delta C_{L,180} = 1.324(1 - e^{-2.308(Re \cdot 10^{-6} - .2)})^{.7262} \quad (25)$$

This equation was created based solely on the information on  $CL_{max}$  mentioned above.

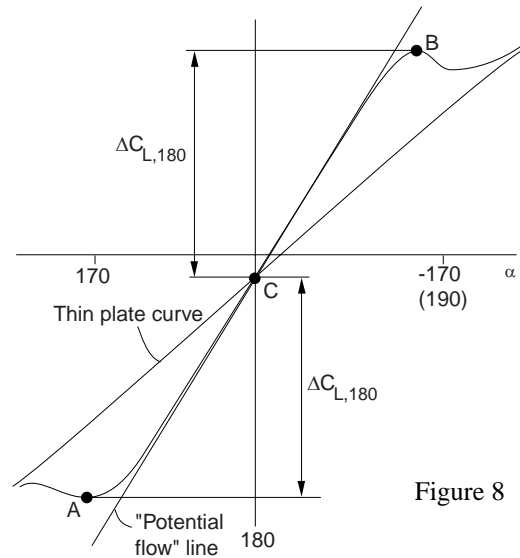


Figure 8



- b. The transition from the linear to the thin plate curve follows the ideas presented in Sect. 2.2.2.
- c. The linear part has a slope  $C_{L\alpha}$  that is, on the average, lower than that of the linear part around zero degrees, see Eq.(12). As a default use:

$$C_{L\alpha,180} = 0.8C_{L\alpha,0} \quad (26)$$

### 2.3 DRAG COEFFICIENT - CD

The drag associated with 90 deg. angle of attack ( $C_{D90}$ ) has a particularly important function in the data conversion. Just like in the case of  $C_L$  the basic thin plate  $C_{D90}$  value is needed to provide the extended  $C_D$  curve.

#### 2.3.1 Finding $C_{D90}$

Ref. [4] provides a method that gives  $C_{D90}$  as a function of radius for any value of the aspect ratio and chord distribution. The essence of Ref. [4] is repeated in algorithmic form as follows.

$$\kappa = \frac{1 - e^{-\frac{20c}{b}}}{2\frac{c}{b}} \quad (27)$$

$\kappa$  is a help variable to be used below.  $c$ ,  $b$  etc are defined in Fig. 9.

$$s = \kappa \cdot c \quad (28)$$

$$n = \frac{C_{D,3D}}{C_{D,2D} - C_{D,3D}} \quad (29)$$

$$C_{D90} = C_{D,2D} \left[ 1 - \left( \frac{s-y}{s} \right)^n \right] \quad (30)$$

Depending on source the values of  $C_{D,2D}$  and  $C_{D,3D}$  can obtain different values.

Ref. 1, Sharp edges:  
 $C_{D,2D} = 1.98$   
 $C_{D,3D} = 1.17$

Ref. 7, 8 and 9, Rounded edges:  
 $C_{D,2D} = 2.06$   
 $C_{D,3D} = 1.45$

Ref. 10: Lower values than those of Ref. 1.

Note that Eq. (30) is valid only when  $y < s$ . Otherwise  $C_{D90}$  assumes the 2D value. The continued discussion is centered around Fig. 9, which also defines some important geometrical quantities used in the formulae.

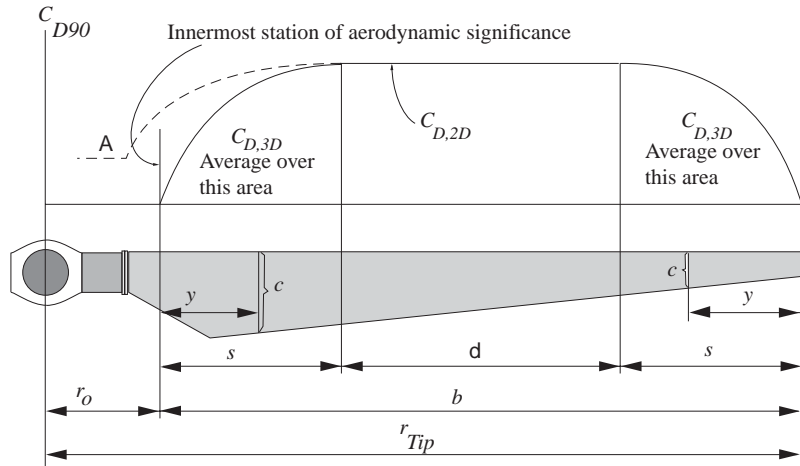


Figure 9

It is assumed that a plate of sufficient slenderness has a certain range where 2D drag is present. Toward the ends the relatively high value of the 2D  $C_D$  can not be maintained because of pressure "leakage" over the tip and root, as seen in the shape of the sketched  $C_{D90}$  curve. A minor complication of low significance is the fact that, at the root end, the drag value can not approach zero because there is not a free end. Rather the shank  $C_D$  should be matched with the 3D curve in order to make a continuous curve. This is indicated by the dashed curve called A. It is, however, recommended that these particular circumstances be ignored. Two reasons for such a recommendation exist.

Firstly there are not sufficient amounts of measured data available to allow a resolution of the problem at such a level. Secondly the contribution to torque from the parts near the root are small. For thrust calculation, however, the full line curve should be changed toward that dashed (curve A). A value of  $C_D = 1.2$  should be a reasonable approximation for the shank part and some hand drawn smoothing toward higher radii in the spirit of curve A should be good enough for thrust calculations. The rest of this report will be focused on the performance aspects of the aerodynamics of the rotor blade.

As pointed out in Ref. [4] the value of  $s$  will have to be found iteratively for any plan form that does not have a constant chord distribution. The significance of the quantity  $s$  is to point out where 3D drag merges into 2D drag as calculated from Eq. (28). The expressions (27) through (30) were originally derived for constant chord plates. In such case the formulae are applicable as written above. If, however, the chord is variable the meaning of the ratio  $c/b$  must be expanded to take into account the variability of the chord. An iteration is necessary. The iteration in search for  $s$  can be carried out as follows.

A small step from the tip of the rotor blade is first assumed. For the corresponding  $y$  value the chord length is evaluated. Dividing by  $b$  yields a ratio that can be inserted in Eq. (27) which is inserted in Eq. (28) to obtain  $s$ . The described action could be thought of as being a step to a radial position  $y$  which is tentatively at  $s$  – but only tentatively. Now  $y$  is checked against  $s$ . If  $y$  is less than  $s$  increase  $y$  a little and repeat the process until a value of  $y$  is found to be equal to  $s$ . Then this is  $s$ -at-the-tip. Correspondingly the root end is analyzed for its value of  $s$ , i.e.  $s$ -at-the-root. The search process is illustrated in Fig. 10.

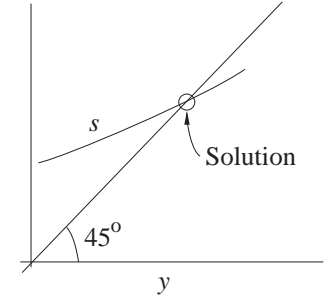


Figure 10

A complicating real effect is that camber and nose radius may modify the value of  $C_{D90}$  as defined above. The reason is that when a wing is blown at 90 degrees onto its bulgy side drag is lower than when blown from the other side. In Ref. [4] the concept of "bulge" is created. It signifies how much the wind facing side deviates from a flat plate. Also the radius of the leading edge is discussed in the same context. Increasing bulge and/or leading edge radius ( $r_{LE}$ ) contributes to reduce the  $C_{D90}$  values by  $\Delta C_{D,round}$ . This also applies to  $C_{D,2D}$  and  $C_{D,3D}$  in Eqs. (29) and (30).

$$\Delta C_{D,round} = -0.83 \frac{r_{LE}}{c} - 1.46 \cdot blg \quad (31)$$

From simple analysis of any wing profile geometry the following relation is deduced.

$$blg = \pm \frac{h}{c} + \frac{t}{2c} \quad (32)$$

where the plus sign is chosen when the wind blows against the suction side. The minus sign is chosen when blown onto the pressure side.  $h$  is the camber line maximum height,  $t$  is the section thickness and  $c$  is chord length. Because of application of different signs on the camber term (first term Eq. (32)) the  $C_{D90}$  drag becomes different for the two sides. But this drag value governs several other aerodynamic quantities. The question then arises, which one of the two values of  $C_{D90}$  to use.

In order to resolve the problem it is proposed to let  $C_{D90}$  vary with the angle of attack. Since we know it has a maximum at +90 degrees and a minimum at -90 degrees a simple sine function comes to mind.

Strictly logically this violates the heuristic definition of  $C_{D90}$  which was meant to be one value. But, reality requires differently. Implementing the simple idea of variation leads to the following expression.

$$C_{D90}(\alpha) = C_{D90,thinPlate} - 0.83 \frac{r_{LE}}{c} - 1.46 \frac{t}{2c} + 1.46 \frac{h}{c} \sin \alpha \quad (33)$$

### 2.3.2 Using $C_{D90}$ to Create $C_D$

The  $C_{D90}$  value is used to calculate the  $C_D$  value of the complete 360 degree range of angles of attack. It determines the amplitude of the thin plate  $C_D$  variation with angle of attack. The thin plate curve is used as a base for the actual blade profile. Following Hoerner[2] or Ref. [4] the drag for a cambered (thin) profile that is completely stalled can be written

$$C_{D,thinPlate} = C_{D90}(\alpha) \cdot \sin^2 \alpha \quad (34)$$

This expression will be used below, but first another technique of describing drag for “low” angles of attack must be established as follows.

The loss in  $C_L$ , see  $\Delta C_L$  in Fig. 11a, can be seen as a deficit in relation to the imaginary continuation of the “potential flow” lift curve depicted as a straight line in the  $C_L$  vs  $\alpha$  diagram. The deficit is the result of first only boundary layer then also separation leading to lesser circulation.

The widening separation region, as  $\alpha$  increases, is also associated with an increasing loss of momentum of the flow, thus drag. By allowing the potential flow line to be integral with the lift curve, for low values of  $\alpha$ , some loss of circulation has already been ignored. The reason is that the boundary layer, how ever thin, generates both drag and loss of circulation. The very small effects associated with the substall angles of attack are filtered away by using the technique of making the line perfectly identical with the  $C_L$  curve where it is straight. This technique also reflects in the  $C_D$  diagram, Fig. 11b, such that  $C_{D0}$  is ignored.

The third diagram in Fig. 11 is a plot of  $\Delta C_D$  vs  $\Delta C_L$  which can be thought of as one separation effect vs another separation effect. It was derived from NACA0025 and -33 airfoils.

Difficulties of a practical nature will arise. The 2D data, as of Fig. 11c, may not extend all the way to where the new  $C_L$  curve reaches. The remedy is extrapolation of the curve in 6c. Investigation, of the nature of this curve, has been carried out by the author previously. For several different airfoils the relationship appeared to be essentially linear. The slope was found to be = 0.13 apart from the bucket seen in Fig. 11c. The bucket tends to appear only for symmetrical and thick airfoils. The explanation is that the thick symmetrical airfoil has separated flow on the upper and lower surfaces at zero  $\alpha$ . As  $\alpha$  increases the lower side separation gradually vanishes while the upper separation does not increase as much as the decrease on the lower side. The net

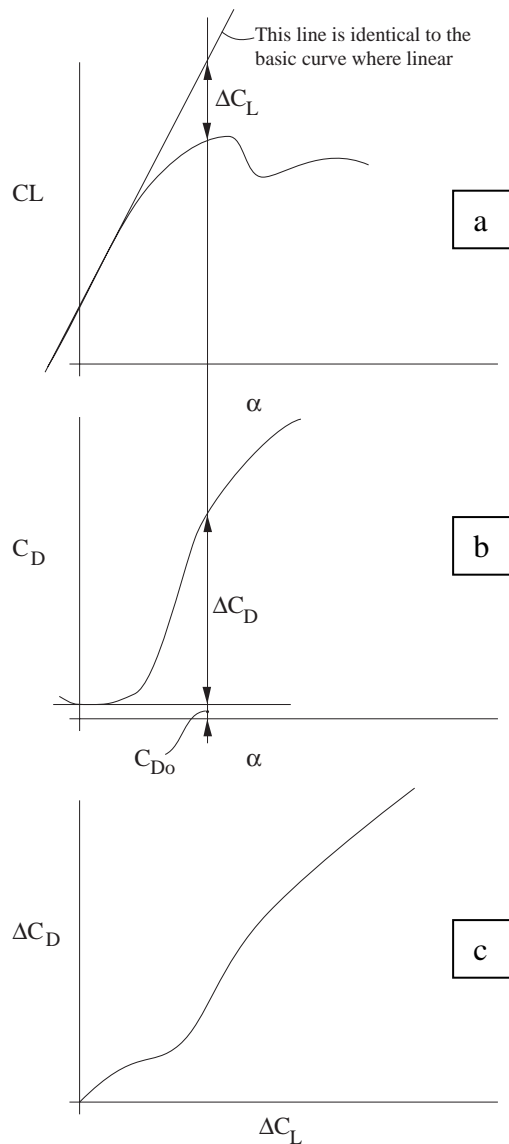


Figure 11

effect is a total lowering of drag. For a regular propeller or wind turbine profile separation is not present on the lower side except for very highly negative alphas. The bucket in the curve seen in Fig. 11c is therefore not present in “normal” airfoils. Pointing to the aberration from normal is intended as a warning that such behaviors may exist and that they are not necessarily the result of error.

The technique used above to calculate the extended  $C_L$  curve can also be used to calculate  $\Delta C_L$  as defined in Fig. 11a. With the curve in Fig. 11c extrapolated this allows calculation of extrapolated values of  $\Delta C_D$  to which an estimate of the friction part of  $C_D$  can be added to yield the total drag estimate. This results in an extrapolated  $C_D$  vs  $\alpha$  table/curve.

We now have two  $C_D$  curves, one coming from extrapolation of the given aerodynamic set, another coming from the completely stalled thin plate. In order to complete the method, the two must now be fused. This is done using interpolation between the two. The interpolation is carried out using the same function  $f$  that was used for the  $C_L$  interpolation, see Eqs. (6) and (10). This technique will accomplish a smooth transition from the given  $C_D$  curve extrapolated to (numerically) high angles of attack. There is admittedly not much theoretical support for the method. Therefore it will be used tentatively until experimental evidence can be used to modify what is proposed here.

In summary the method can be expressed as follows.

- Determine  $\alpha$
- Use the corresponding value of the potential flow  $C_L$  and subtract the  $C_L$  value to get  $\Delta C_L$
- From the extrapolated  $\Delta C_D$  vs  $\Delta C_L$  curve (see Fig. 11c) get  $\Delta C_D$
- Add estimate of the friction value of  $C_D$ , i.e.  $C_{D \text{ friction}} = .006$  around  $\alpha = 0$  and  $C_{D \text{ friction}} = 1.25(t/c)^2$  (Hoerner p. 6-20) around  $\alpha = 180$  with arbitrary fairing between. Define  $C_{D e} = \Delta C_D + C_{D \text{ friction}}$
- The final drag value is obtained using the function  $f$  from Eq. (6):

$$C_D = f \cdot C_{De} + (1 - f) \cdot C_{D, \text{thinPlate}} \quad (35)$$

At around 180 degrees of  $\alpha$ . There are special circumstances valid for drag whose practical importance can be ignored. It is therefore suggested that the thin plate  $C_D + 1.25(t/c)^2$  be used in that alpha range.

## 2.4 MOMENT COEFFICIENT - $C_m$

### 2.4.1 Aerodynamic Centers

In the basic inviscid theory for thin airfoils the 25% chord position (AC) emerges as the prominent point. The lifting force, perpendicular to the undisturbed flow direction, acts through this point denoted AC in the adjacent figure. The simple theory only predicts real behaviors for a limited angle of attack range as symbolized in Fig. 12a. At increasing angles the theory becomes increasingly inaccurate and nature follows laws other than those based on simple linear theory. This has to do with stall, which is a viscous phenomenon.

The 25% point is generally made reference to as the aerodynamic center. But there is also another center (CC) namely that point through which the camber lift ( $C_{Lc}$ ) contribution acts. The camber lift is present even at  $\alpha = 0$ . When  $\alpha$  is varied the additional lift acts through AC while the camber lift is essentially unperturbed and still located in CC. This is typically valid for the situations according to a and b. In the flow situation as in c measurements must be carried out since this is far from the linear angle of attack range. At d and e the flow resembles that at a and b meaning that now the AC point is still 25% from the edge that faces the

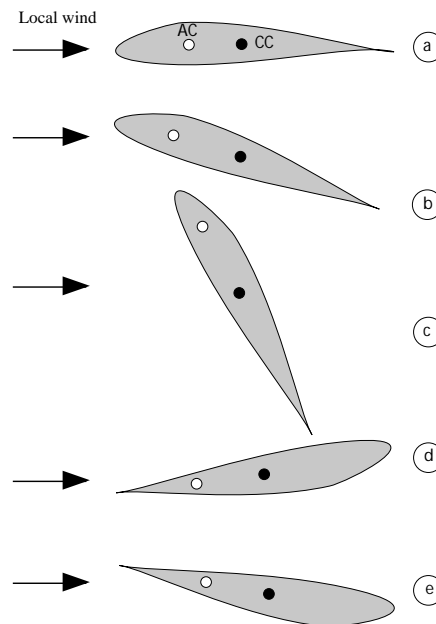


Figure 12

wind. But, this means that in the same coordinate system the arm length, counted from the rounded edge is 75% chord length. It is also assumed that the camber lift acts through the very same CC point as in a and b. Using the angle  $\beta = (\alpha - 180)$  instead of  $\alpha$ , the profile, blown from behind, can be seen as a profile with the approximate lift

$$C_L = 2\pi\beta \quad (36)$$

Attention must be paid to the angle, which, in this case, should vary from zero to 360 degrees in order for the lift to obtain the correct sign.

#### 2.4.2 Moment Arm and its Relation to CL and CD

With an idea of the camber lift and  $C_L$  at around 180 degrees, the moment can be modeled and therefore also the moment arm. This is to say that now we have information about the moment and its arm at around 0 and 180 degrees. To complete the model information is required for the other alpha regimes. These are, loosely speaking, from 18 to 174 negative and positive angles. Critzos' report, see the reference list, shows the variation of  $C_L$ ,  $C_D$  and  $C_m$  from 0 to 180 degrees for the symmetrical airfoils NACA0012 and NACA0015. An evaluation of the moment arm has been carried out for these data. A description of the method follows.

First the basic assumption is made that both lift and drag act through the same point (P) on the chord line. This assumption is somewhat arbitrary simply because the chord line is arbitrary and it can be shown that P lies above (toward the humped suction side) the normal definition of a chord line. This should not disturb the usage of the basic assumption, however, as explained further down the text.

The moment, on coefficient form, is defined around the 25% chord point. Thus lift and drag contribute to create the moment accordingly.

$$C_m = (-C_L \cos \alpha - C_D \sin \alpha)(arm - .25) \quad (37)$$

The arm length is solved from this expression.

$$arm = \frac{C_m}{-C_L \cos \alpha - C_D \sin \alpha} + .25 \quad (38)$$

If this arm length were to be used to calculate  $C_m$  according to Eq. (37) then the exact input value of  $C_m$  would be regenerated. This is pointed out with the perspective that the point CC might not be positioned exactly on the chord line, although that was the initial assumption. Thus, using this technique consistently yields the correct value of  $C_m$  and what has hitherto been called arm can be thought of as a work parameter used to calculate correct values of  $C_m$ .

The work parameter arm was calculated from the Critzos data for two airfoils whose data were given in his report. The corresponding graphs are seen in Fig. 14. This graph also shows one corresponding  $C_L$  curve for orientation. The fact that the end points do not hit the 25% and 75% points respectively is caused by numerical effects where

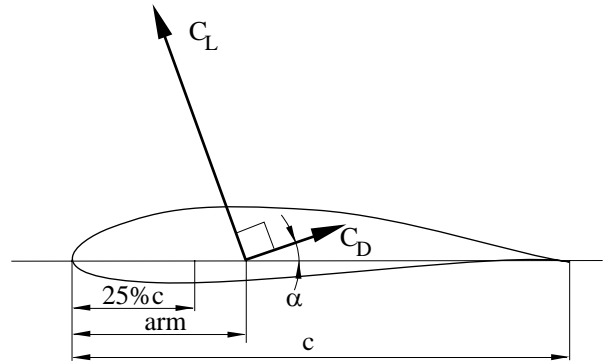


Figure 13

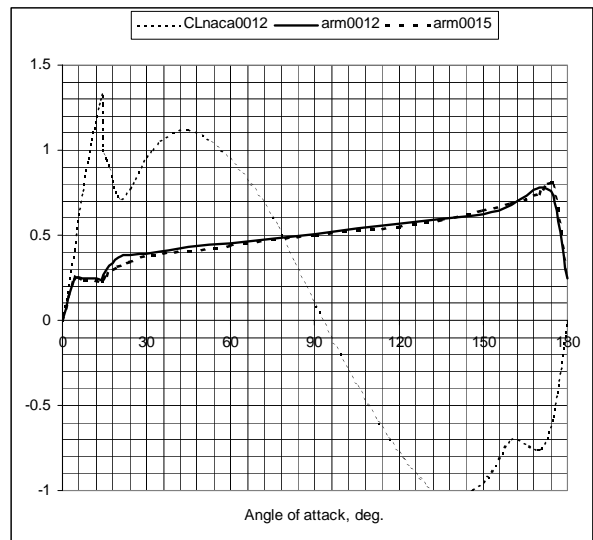


Figure 14

both  $C_L$  and  $C_m$  are zero. The data at  $\alpha = 0$  and  $\alpha = 180$  are therefore to be ignored.

The very straight line segment, the deep stall region, from about 20 deg. to 160 deg. is noteworthy. It suggests modeling with a straight line with a certain slope and offset from the origin. The fact that the end points do not hit the 25% and the 75% levels respectively is caused by numerical effects with no consequence for the calculation of  $C_m$ . The reason is that  $C_m$  is calculated with another method at around zero and 180 degrees, as dealt with later in the text.

It should also be pointed out that, although the  $C_L$  and the  $C_D$  data for the two airfoils are quite different, the assumptions lead to a remarkably similar result in terms of moment arm length.

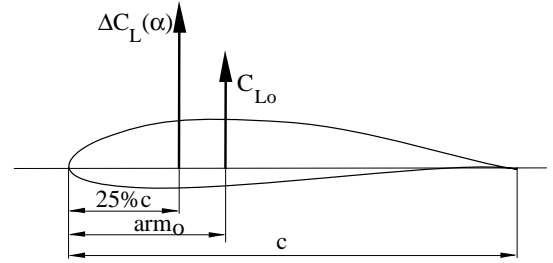


Figure 15

One assumption, that will turn out useful when modeling the general airfoil  $C_m$  behavior, is to say that, at the linear range of  $\alpha$ , camber lift is constant. Furthermore, the lift vector from pure camber acts through a constant chordwise position independent from  $\alpha$  variations. This is the lift vector, that gives rise to the zero moment coefficient. One illustration of this assumption is the moment arm calculation compared to that “measured”. The data were taken from Rep. FFA TN 1990-15 valid for NACA63-415. The comparison is seen in Fig. 16.

The “measured” arm length was generated from  $C_L$ ,  $C_D$  and  $C_m$  using Eq. (38). The calculated arm length was arrived at in the following manner.

It was assumed that the  $\alpha$  dependent part of the lift goes through the 25% chord point. At  $\alpha=0$  the lift coefficient is called  $C_{L0}$ . Its arm length is obtained from

$$arm_0 = 0.25 - \frac{C_m(\alpha = 0)}{C_{L0}} \quad (39)$$

which is the same expression as Eq. (38) ignoring  $C_D$ . For the moment coefficient, referred to the leading edge, Fig. 15 then gives

$$C_L \cdot armCalc = 0.25\Delta C_L + C_{L0} \cdot arm_0 \quad (40)$$

Noting that

$$C_L = \Delta C_L + C_{L0} \quad (41)$$

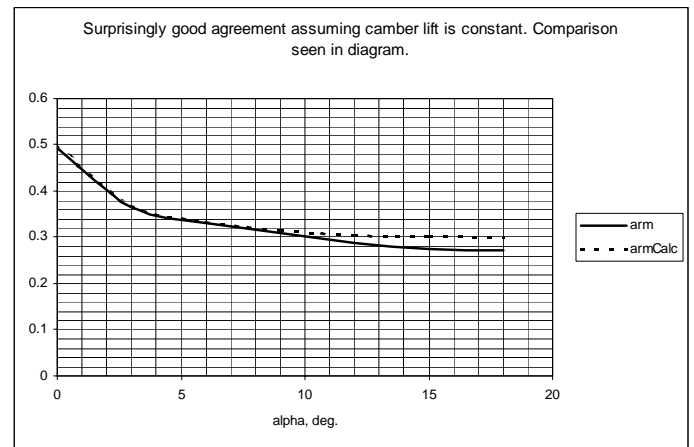
the arm length becomes

$$armCalc = \frac{0.25(C_L - C_{L0}) + arm_0 C_{L0}}{C_L} \quad (42)$$

The two arm lengths from Eqs. (38) and (42) are plotted in the same diagram, see Fig. 16. The graph reveals a few characteristics of particular interest.

- The theoretical curve tends to become relatively higher as stall is approached
- The agreement between “measured” and calculated is generally quite good in this range.

Figure 16



Point a) can be explained by the fact that the NACA63-415 airfoil is more rounded than NACA0012 on the suction side. NACA63-415 should therefore be expected to stall such that the separation point moves gently from the trailing edge as  $\alpha$  increases. This means that suction is maintained over a larger forward

part of the airfoil, thus generating more of its lift at a more forward position. This lift will thus act through a point located forward of the 25% point. I.e. a short moment arm length should be expected.

Also it can be expected that the separated rear flank of the airfoil represents drag, because full pressure recovery is not achieved in a separated region. The drag center is thus positioned above the chord line, for moderate  $\alpha$ s, which would have given a nose-up moment contribution if  $\alpha$  is about = 0. But, for increasing  $\alpha$ s, the drag line will increasingly fall below the 25% point. That translates into a nose-up contribution as well. Therefore, the simplified approach, neglecting both the travel of the vector corresponding to  $C_L(\alpha)$  and the influence of  $C_D$ , gives too large an arm.

The described effect should go away as 90 degrees and higher are entered. There is no particular reason to assume that a cambered airfoil at say 100 degrees should differ from a symmetrical airfoil in this respect. Therefore it is assumed that the “arm line” from the cambered airfoil will merge with that of the symmetrical airfoil. The technique to accomplish this effect is dealt with below.

The curves from Figs. 3 and 5 are sketched into the same diagram, see Fig. 17. For low angles of attack the simple calculation curve is valid. At some slightly undetermined point P the straight line should gradually become dominant. Thus an interpolation function could in principle be applied to accomplish the transition from P to Q. However, since the situation is complicated on the negative side ( $\alpha < 0$ ), where there are two singular points, the blending of curves is not done for the arm function. The blending is instead best applied to the moment coefficient directly. Thus  $C_m$  in the linear range is blended with  $C_m$  calculated from Eq. (37). The function performing the fusing of the two curves can be written as follows.

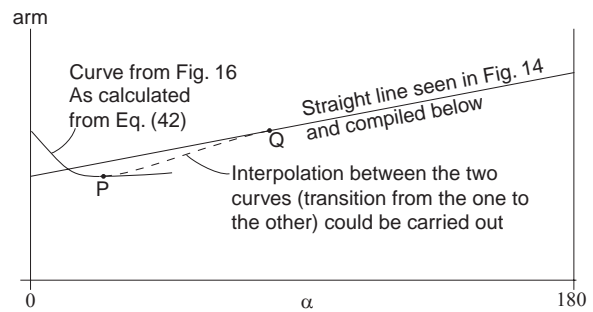


Figure 17

$$arm = (1 - f)theCurve + f \cdot armLine \quad (43)$$

where the function  $f$  will be determined below.

This simple approach grew into a model upon discovery of a Chinese report from CAARDC where several airfoils were investigated in “some” tunnel at Reynolds numbers about half a million. The report is written in Chinese so the background material is not available to a western civilization engineer. But, numbers and graphs are the same in the two cultures and the plotting of arms for a selection out of the Chinese report appears in Fig. 19. The plot has the same axes as those seen in Fig. 14. The Excel plot also includes the NACA 0012 and 0015 data as seen above.

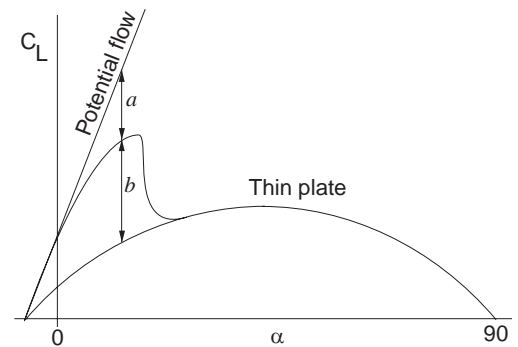


Figure 18

One slightly disturbing feature of the Excel plot is that the airfoils tested in the Chinese wind tunnel appear to group nicely around an essentially straight line, while the NACA data for 0012 and 0015 seem to form a family of their own. It is not clear what constitutes the essential difference. The author looked for differences in Reynolds number and aspect ratio of the different models, without being able to deduce an explanation for the discrepancy. Since, however, airfoils on horizontal axis wind turbines are always cambered the modeling technique, as indicated in Fig. 17 and Eq. (43), will be derived from the Chinese set of curves.

One important systematic effect in the curves seems to be that the approach behavior of the arm curve to tend toward the straight line is similar to that of the  $C_L$  curve. When the  $C_L$  curve leaves the potential flow

linear part it tends toward the thin plate curve in like manner. This observation can be used to create a model for the function  $f$  in Eq. (43) as follows.

If the arm curve is to approach the straight line as fast as the  $C_L$  curve approaches the thin plate (stalled flow) curve. In fact, after numerical experimentation, an improvement could be achieved if the approach also included a square relationship as follows.

$$f = \left( \frac{a}{a+b} \right)^2 \quad (44)$$

After the lift calculations have been carried out, both  $a$  and  $b$  will be available. The same technique is to be used even for the linear lift range around  $\alpha = 180$  degrees.

The straight line representation with reference to Fig. 14 and Fig. 19 is

$$armLine = offset + slope(\alpha - 90) \quad (45)$$

The offset and slope were found after some experimentation using an Excel sheet.

$$offset = .5111 - .001337 \cdot \alpha_0 \quad (46)$$

$$slope = .001653 + .00016 \cdot \alpha_0 \quad (47)$$

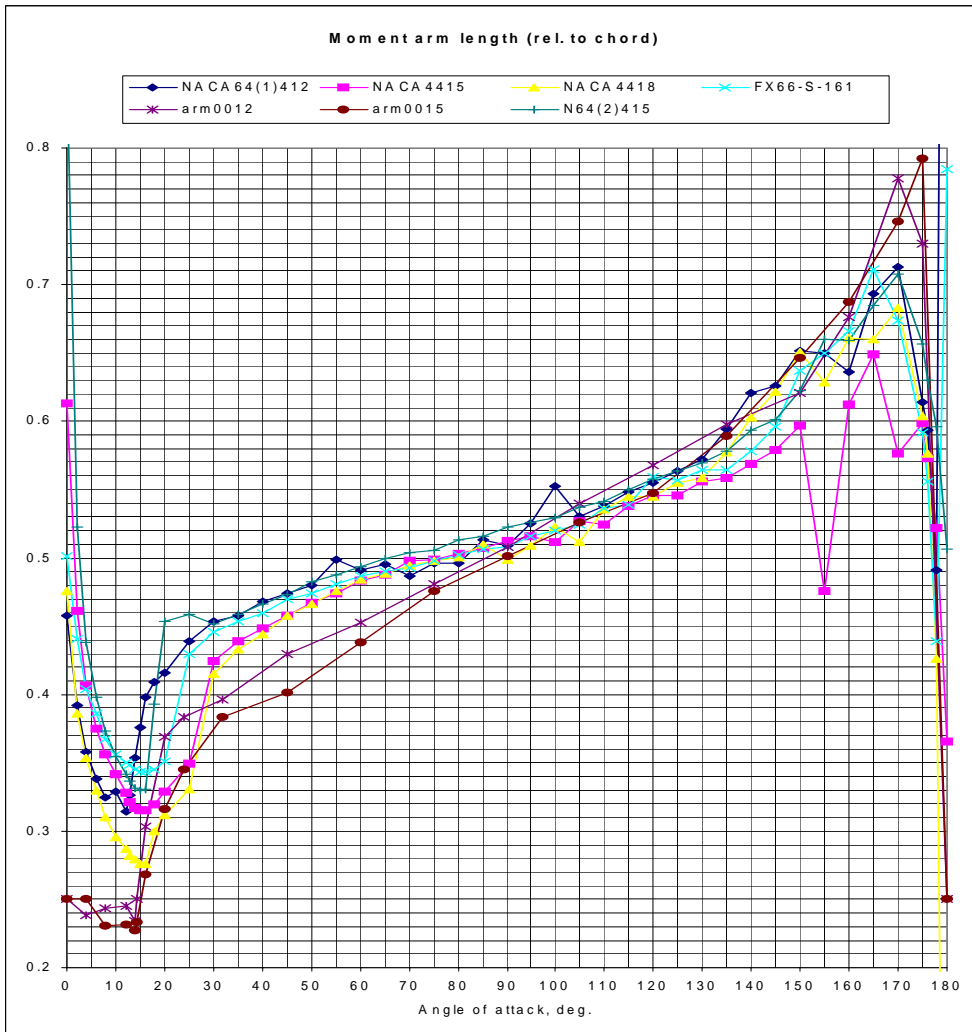


Figure 19



where  $\alpha_0$  is normally a negative number.

The proposed approximation technique was tested numerically on an Excel sheet. It was then discovered that Eq. (42) can be improved somewhat if the whole expression is multiplied by a factor. The new expression, that replaces that of Eq. (42), then reads

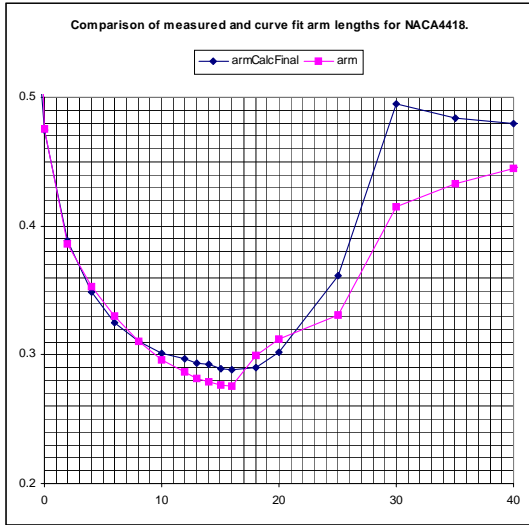


Figure 20

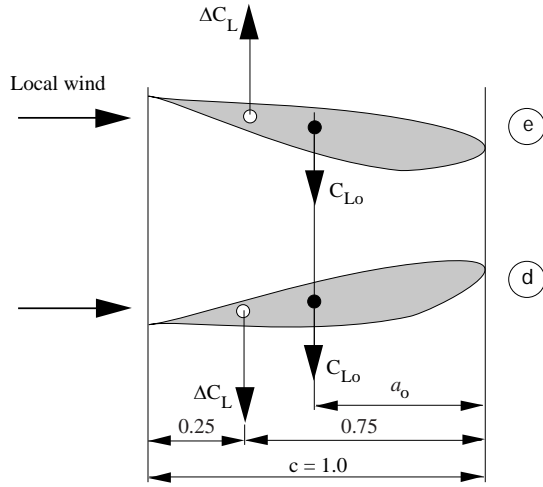


Figure 21

$$armCalc = \frac{.25(C_L - C_{L0}) + arm_0 C_{L0}}{C_L} \left\{ 1 - .2 \left( \frac{\alpha^\circ}{18} \right)^2 \right\} \quad (48)$$

One example of comparison was made for NACA4418. The graph appears in Fig. 20.

The striking difference at 30 degrees is explained by the fact that the predicted thin plate curve turned out to be higher than the CL curve in deep stall from the Chinese measurements. There is, however, no firm indicator how to use this information. Therefore it is ignored.

To complete the full 360 degree range with respect to  $C_m$  the same technique can be employed.

In Fig. 12,d (or 21d) the angle can be made greater than that in 12,e (or 21e) before separation occurs. This can be realized when thinking of the air as having difficulties rounding a sharp corner. A sharper rounding of the corner is required at a numerically lower negative  $\alpha$  than correspondingly for a positive angle. This is to say that the active linear range is larger just below 180 degrees than above. But angles above +180 degrees will be translated into negative angles in the range of say from -165 to -180 degrees. This should reflect in the linear function that is called *armLine*, see Eq. (43). An asymmetry arises in terms of the linear function such that its behavior on the negative side behaves as indicated in Fig. 22.

The moment coefficient contribution from the *arm* function will be calculated from Eq. (37). However, for the linear range of angle of attack the moment coefficient is calculated from the indication in Figs. 36 and 45. Taking the 25% point as the reference point, as usual, yields

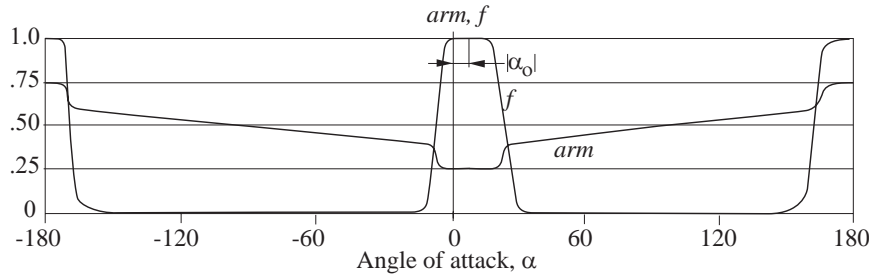


Figure 22

$$\text{Near } \alpha = 0: \quad C_m = -a_0 \cdot C_{L0} \quad (C_{L0} \text{ is a pos.number}) \quad (49)$$

$$\text{Near } \alpha = 180: \quad C_m = -0.75\Delta C_L - a_0 \cdot C_{L0} \quad (C_{L0} \text{ is a pos.number}) \quad (50)$$

where, in this case

$$\Delta C_L = C_{L\alpha} \cdot (180 - \alpha) \quad (51)$$

where  $C_{L\alpha}$  is obtained from Eq. (12).

From the linear range toward deep stall (on the negative side as well as on the positive side) there is a transition toward a line when the moment is expressed as an arm length rather than a coefficient. The linear arm function obtains its form as seen in Fig. 22. Because the airfoil is not symmetrical there is an asymmetry in the arm curve as well as in the transition function  $f$ . It can be noted that an exercise in calculation, of the arm length on the negative side, gives two singular points for  $C_m$  e.g. where  $C_{L0}$  equals  $\Delta C_L$  and the two are of opposite signs. Therefore, when they are added to yield the total  $C_L$  value, see Eq. (41), the sum is zero but the  $C_m$  value is finite. The equation for the calculation of the arm, according to Eq. (42) explodes at that point because  $C_L = 0$ . A similar situation exists near  $-175$  degrees.

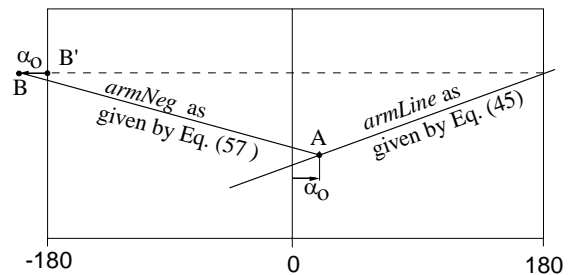


Figure 23

Obviously the calculation of  $C_m$  in the immediate vicinity of the singular points will give very unreliable values when the arm method is used. Fortunately there is a different method available near these points, e.g. Eq. (49) and (50). In deep stall this difficulty does not exist. There the straight line arm method is the only one available.

Because of sparse availability of deep stall data (the Chinese report does not deal with the negative side) the negative side straight line (Fig. 22) is uncertain except for the case where the airfoil is symmetrical. Then also the curves in Fig. 22 are symmetrical. It is, however, appealing to use the straight line arm function to calculate  $C_m$  even for cambered airfoils.

From the described uncertain background the left part of the diagram in Fig. 22 must now be constructed. This is done from the observation that both of the curves for  $C_L$  and  $C_D$  are “compressed” for positive  $\alpha$  when the airfoil is cambered (compared to a symmetrical airfoil). This should reflect on the negative side as an “extension” of the corresponding line. In Fig. 23 it is seen how the end points of the line on the negative side are constructed. As a consequence its function form is a straight line through the points A and B as governed by the zero lift angle of attack.

The algorithmic presentation of the calculation of the line on the negative side follows.

$$x_A = |\alpha_0| \quad (52)$$

$$y_A = \text{armLine}(|\alpha_0|) = \text{offset} + \text{slope} \cdot (\alpha - 90) \quad (53)$$

$$x_B = -180 - |\alpha_0| \quad (54)$$

$$y_B = \text{armLine}(180) = \text{offset} + \text{slope} \cdot 90 \quad (55)$$

$$k = \frac{y_B - y_A}{x_B - x_A} \quad (56)$$

$$\text{armNeg} = y_A + k \cdot (\alpha - x_A) \quad (57)$$

### 2.4.3 Summary of the $C_m$ Calculation Technique

The building blocks in the method to produce an approximation for the  $C_m$  curve through 360 degrees can be described with the following statements.

1. The  $C_m(\alpha)$  curve can be generated from:

- a.  $C_m(\alpha_1)$  where  $\alpha_1$  is an arbitrary angle of attack near zero
- b.  $C_L(\alpha_1)$  must be known
- c.  $C_L(\alpha)$
- d.  $C_D(\alpha)$

2. The basic data used are from Critzos [1] – NACA0012 and NACA0015 and Chinese data [12] for several cambered airfoils, although only data for positive angles of attack exist in the Ref. [12] report.

3. The technique used relies on thin airfoil theory for small numerical values of  $\alpha$ . For deep stall data the arm from the leading edge to the center of lift and drag was extracted from the measured data. This arm is cast in a curve fit formulation. Knowing  $C_L$  and  $C_D$  in this deep stall region allows the calculation of  $C_m$  using also the arm information. In the region between small values of  $\alpha$  and deep stall a *transition* based on the shape of the  $C_L$  curve is applied.

4. After step 3 a  $C_m$  curve has been generated. However, at around zero degrees angle of attack there is usually original data available. The original data should of course be used where available and a transient to  $C_m$  data according to the method above should be applied.



### 3. END EFFECTS

#### 3.1 OVERVIEW OF END EFFECTS

The blade is exposed to a flow that becomes more three-dimensional (3D) as the tip or the root is approached from some inboard radius. The effective parameter to measure three-dimensionality is the ratio (local chord)/(distance to nearest end).

Blade Element Momentum (BEM) theories rely on aerodynamic information in the form of tables, which in turn depend on the profile shape. Since a profile is a two-dimensional (2D) concept so is the aerodynamics. Therefore the unmodified 2D tabled aerodynamic coefficients are not suited to be used directly near the ends of a blade. In BEM theory 2D profile aerodynamics is used because this is inherent in the method. But, compensation for 3D effects can be introduced by changing the aerodynamic tables in a dedicated way.

The effect from the radial pressure gradient is that, close to the ends of the blade, the lift slope and the drag value at 90 degrees angle of attack tend toward zero as the tip, or the root, is approached. The drag value at 90 degrees angle of attack has a crucial role in the creation of the 180 degree tables as explained in Sect. 2. The end effects, as described, will be referred to as “gradient effects”, or “gradient corrections” when applied as increments to basic two-dimensional aerodynamic coefficients.

Superimposed on the gradient effects is the Himmelskamp effect. It will be taken into account as an increment as explained below. Its most prominent feature is to increase maximum  $C_L$  to about twice its 2D value.

When running a performance/aeroelastic program, the gradient corrections are best implemented directly in the files that contain the aerodynamic information, while the Himmelskamp effect could be calculated on line. Thus, the Himmelskamp effect could be implemented in the coded algorithms in the program. Even if a blade has pitchable tips, for run-away control, the tip effects are favorably given from the beginning. This is because only chord in relation to radial position matters (not pitching). In the case of the extremely remote possibility of variable chord or radial extensibility, for control purposes, would the gradient effects be implemented as code, on-line.

The Himmelskamp effect depends on RPM such that, below a very low RPM, there is no effect, while above this very low value there is full effect. This apparent step in Himmelskamp functionality is not truly a step. In reality the effect rises softly but distinctly at some low value of RPM. In practical computer implementation a relatively fast rising curve fit equation is applied, which rises from 0 to 1 over some suitably chosen low RPM. This allows simulation of starts and stops. The RPM dependent characteristics of the Himmelskamp effect thus suggests implementation in the code rather than in the fixed aerodynamic tables, although there would hardly be any noticeable difference in the resulting loads if implemented in the tables.

#### 3.2 GRADIENT EFFECTS

Near the tip both lift and drag deviate from what would have been the case in the 2D situation. These effects have in fact already been covered as far as the flat plate aerodynamics are concerned, see Sect. 2. In that section, however, the end effects were not explained explicitly. A practical problem must be overcome as follows.

In the method for lift calculation the  $C_L$  curve is extended using an interpolation technique in which the flat plate curve amplitude is determined by the  $C_{D\ 90}$  value. But, since the  $C_{D\ 90}$  value is a function of the nearness to the end, the complete  $C_L$  curve must be affected by tip proximity. In experiments, e.g. Ref. [11], the linear range lift has been observed to be affected by tip proximity. It is assumed that  $C_{Lmax}$  is subjected to the same effect. These measurements depend on a notion of the angle of attack. The angle of attack will always have to be calculated even in the case of measurements. Therefore, the “measured” angle of attack, as it were, is prone to errors inherent in the estimation method.

But, in practical engineering evaluation, of rotor performance, angles of attack will have to depend on the methods that we know of today. So, if there is an error in the estimate of the angle of attack, this error can be accounted for by modifying the corresponding  $C_L$  value. This process has given  $C_L$  vs  $\alpha$  curves, which appear to have lesser slopes than those two-dimensional. In a coherent methodology, using the available methods for angle of attack evaluation, it is therefore relevant to consider even reducing the linear range slope of a  $C_L$  vs  $\alpha$  curve. Some measurements even seem to indicate that the lift at zero angle of attack is higher in this case. The method of this document will rely on one tip proximity decrease of loading for attached flow and another for totally detached flow. All situations between these extremes will be described by interpolation.

### 3.2.1 Tip Effects – Attached Flow

Steady state blade pressure data were obtained in the CARDC wind tunnel from the FFA model wind turbine rotating in polar symmetric flow. For a description of these tests and corresponding analysis, see Ronsten [14] - [16]. These data have been reexamined, in the development of this report, with the purpose to look for tip effects in order to model these. From Ref. [14] it seemed that only the two outermost stations produced data that pointed to an effect. The two tip-most stations from Fig. 9, in the reference, are reproduced in the figures below. These stations were located at 97.5 and 99 % of tip radius. The station at 97.5 % showed no evidence of any tip effect at all. However, some further analysis of the data files revealed that, in some cases, where the blade is more highly loaded, the tip effects extend further inboard. Such is the case particularly for cases 38 and 39 (definition in Ref. [16]). For case 38 a significant difference is seen over the full length of the blade while at case 39 only the four outer  $C_p$  distributions are different. The expectation is that case 39, which represents the highest possible loading (i.e. it contains most stall), should be the one displaying more of differences. But, there is the difficulty of assessing the angle of attack correctly, which might explain the discrepancy.

The test information essentially consists of pressure distributions from 29 orifices around the perimeters of 8 airfoil sections, at different radii, of a 2.5 m long blade, of about 1985 vintage, manufactured by Stork of Holland. The pressure tapped radial stations were densely packed in the proximity of the tip.

To carry out the numerical analysis, of these data, the following sequence of thoughts was used to create a practical engineering model, whose purpose it is to allow correction of standard 2D aerodynamic tables to 3D equivalents to be used in loads and performance calculations of the BEM type.

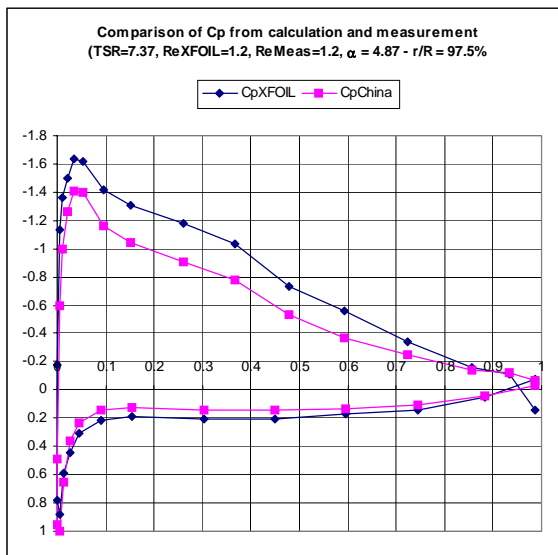


Figure 24

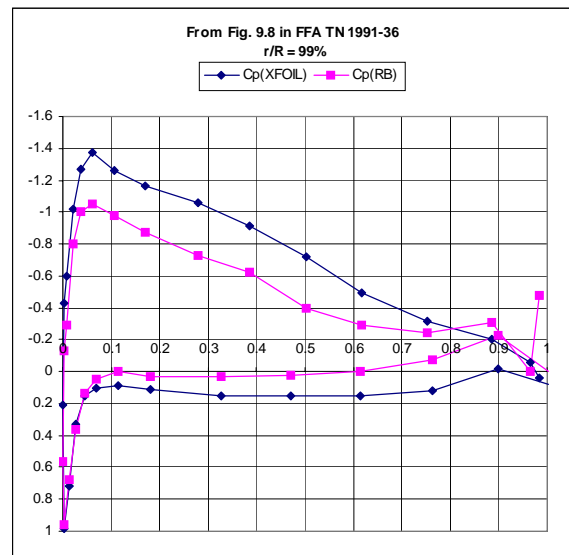


Figure 25

First the assumption is made that the vertical dimension (y direction in the profile coordinate system) can be ignored when integrating the moment. Properly done the pressures should have been integrated around

the profile geometry to yield the normal coefficient (CN), the tangential coefficient (Ct) and the moment coefficient (Cm). But, since the profiles are close to the tip, they are relatively thin making the approximation acceptable for the intended purpose. Therefore, the method was to calculate the incremental forces on a flat plate of no thickness. This makes it possible to calculate CN and Cm (not Ct). In other words the pressure coefficient Cp is multiplied piecewise by the dimensionless chord distance between orifices to build up the CN value. Similarly for Cm where of course multiplication by the length of the arm to the quarter chord point is included in the calculation. The described method, applied to the data of the two figures above, gave the following numerical values.

Table 3.2.1 - 1

r/R location	Non-rotating - XFOIL			Rotating - Measurement		
	CN	Cm	Arm from 25% chord	CN	Cm	Arm from 25% chord
97.5% ( $\alpha=4.9^\circ$ )	.916	-.0906	.099	.708	-.0698	.099
99% ( $\alpha=3.6^\circ$ )	.818	-.0814	.100	.497	-.0241	.0484

A study, of the background numerical files, reveals that at 95 % of radius there is no significant difference between non-rotating (XFOIL as well as non-rotating measurements) data and rotating (measured) data. At lower radial positions, however, the measurements yield higher values of CN. This can be interpreted as an error of the lifting line (LL) method for angle of attack evaluation. Selected data, from the FFA non-rotating measurements, appear in Fig. 26. The global parameters behind the case numbers are defined in Ref. [16].

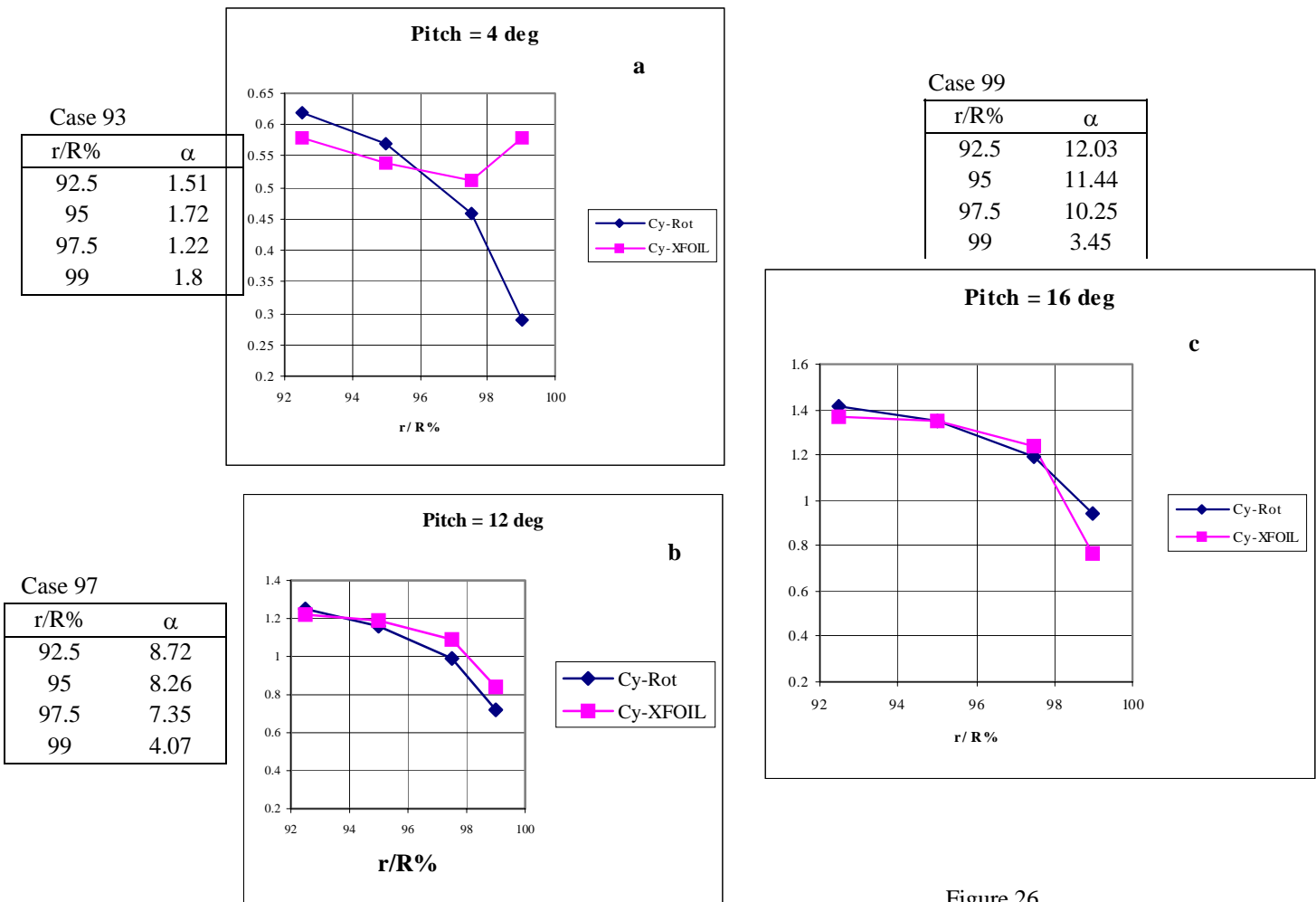


Figure 26

If it is assumed that the angle of attack error from the LL method could be eliminated then the calculated curves (squares) could be moved up to match the near two-dimensional data that should be present at say 75 to 80% of tip radius. It is then seen more clearly that, in relation to measured data, the calculated curves do not drop off toward the tip as they should.

The non-rotating data seen in the three samples above are usable as rotating data below stall. The matter is complicated by the fact that when the profile is partly or fully stalled there are no 2D data in that region if the blade rotates. The explanation can be found in the intricacies of the separated flow being propelled toward a higher radius, thus contributing to a centrifugal pumping action with the flow being essentially radial. Since the data above comes from the non-rotating tests they can only be representative for rotating conditions if the flow is attached.

The relatively small radial extent of discrepancy, as evidenced in the three charts, can be compared to findings in Refs. [17] and [18], where the region of tip flow appears to be somewhat larger.

In the table, including  $C_m$  numbers above, it is seen that at 97.5% there is a difference in CN, but the difference in moment arm is insignificant. This means that  $C_m$  scales linearly with CN, and probably with CL as well. At the 99% station the table values give evidence of significant differences in all parameters. This should be expected since the flow is far from being two-dimensional. For a load calculation it can be concluded that it is quite satisfactory to scale the moment as the CN value scales, i.e. the ratios, between the 2D value of the aerodynamic coefficients and the 3D ditto, have the same values – equal for CN and  $C_m$ .

It is encouraging to notice that the  $C_p$  data from the rotating measurements are practically identical to those measured on the fix mounted blade in the FFA wind tunnel, when the Ronsten pressure pattern fitting technique is successfully applied. This statement holds for all instrumented stations except for the 30% r/R station provided the flow is attached. However, for the purpose of comparing results from XFOIL, the local angle of attack must still be estimated, thereby introducing a source of errors. Even so, it is surprising how well the XFOIL data, in most cases, fit the measured data.

For the purpose of paving the way for a model of calculation, the following set of observations and conclusions is stated:

*Attached flow:*

1. Rotation has hardly any influence of practical importance on the sub-stall flow near the tip.
2. The three-dimensional effects at the tip must be of a potential flow type.
3. Only a certain small outboard part of the blade is affected by tip proximity effects.
4. The extent of the affected span is probably a function of loading. This dependence will be ignored.
5. The tip effect on drag is unknown.

*(Partly) separated flow:*

6. At 90° angle of attack, the tip proximity effects seem to extend much further inboard than in the attached flow case. Here the rules of Section 2.3.1 (“Finding CD90”) apply.
7. In partial separation interpolation must be carried out.

The calculations described above, together with the statements 1 - 6, constitute the basis for model making. It can be reasoned as follows.

The outermost 8%, that seem to be affected by tip effects, are valid for the particular Stork blade used in the tests. But, a connection to other plan forms must be made. To assist in such a task the adjacent picture can be used.

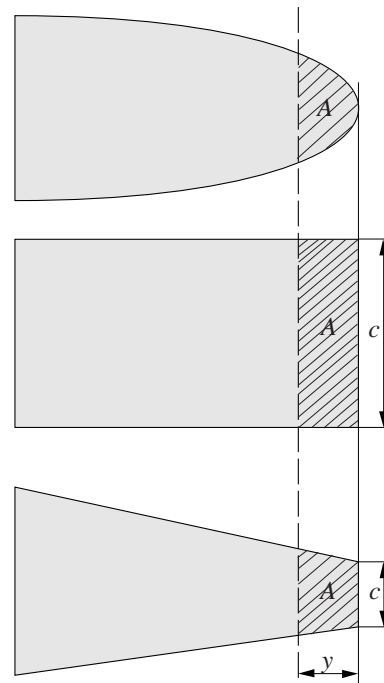


Figure 27



All three plan forms have the same distance from the tip to the dashed line. Although this measure is identical in all three tips it certainly appears that the mid-figure has its dashed line effectively closer to the tip than the two other shapes. It may be less obvious that the top shape has the dashed line effectively closer to the tip than has the lower shape. The distance  $y$  is the same but the surrounding geometry is different in all three cases, which will be used to serve as representatives for all existing shapes of tips.

To capture these intuitive thoughts into something more tangible the concept of “local aspect ratio” comes to mind. The serrated areas ( $A$ ) have different aspect ratios and, as inspired from airplane practical aerodynamics, the *local aspect ratio* can be expressed as  $y^2/A$ . Therefore the idea can be expressed as follows:

*Points of equal influence, from three-dimensional effects near a tip, are calculated from equal local aspect ratios.*

In practical application the Stork data will be plotted versus local aspect ratio rather than versus radius. Then that plot is assumed to be valid for all possible blade shapes. This completes the creation of the model for the effective coordinate as a technical measure of tip proximity. The practical consequences remain.

The  $C_N$  vs radial coordinate in the plots above only show convincingly that from about 95% of tip radius to the very tip the  $C_N$  value, i.e. the loading, is attenuated by a factor that is roughly one near 95%. It is equal to zero at the very tip. Deviations at lower radial coordinates are probably caused by error in the estimate of the angle of attack. The model therefore becomes to multiply the 2D  $C_L$  and  $C_m$  tables by a factor, which is constructed as a curve reminiscent of a quarter circle according to the Fig. 28. The figure is a more general transformation of the information where local aspect ratio (LAR) takes over the role of  $x$  coordinate. To use this information the following steps could be taken.

1. Assume that the aerodynamic table definition is required at some radial location  $r$  corresponding to  $y = R_{tip} - r$

2. Calculate  $y_1 = \sqrt{A} \dots$  (using  $LAR_0 = 1.0$  for attached flow) (58)

3. Compare  $y$  with  $y_1$ . If  $y < y_1$  go to the next step, else there is no modification to the two-dimensional aero tables.

4. Calculate  $LAR = y^2 / A$  (59)

5. Calculate the factor  $g = g(LAR) = \{1 - (1 - LAR)^e\}^{1/e}$  (60)  
where  $e=2.5$  was found to be a suitable value.

6. Apply the factor to the 2D values of  $C_L$  and  $C_m$  but not to  $C_D$ . Thus for all angle of attack values in the 2D aero table do:

$$C_{L,3D} = g C_{L,2D}; C_{m,3D} = g C_{m,2D}; C_{D,3D} = C_{D,2D} \quad (61)$$

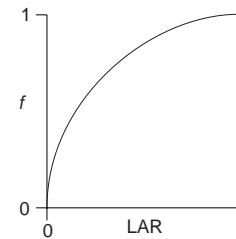


Figure 28

### 3.2.2 Tip Effects – Detached Flow

Ref. [20], (measurements on the NREL 10m diameter machine) indicates that when the outer part of the blade starts experiencing separation the decline of maximum loading is vaguely visible at 80% radius. There was unfortunately no instrumented station at a higher radius on the blade. This corresponds to a LAR of approximately 2.2.

Thus, the tip effect is more pronounced in the case of separated flow being

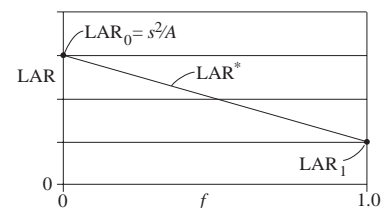


Figure 29

visible at  $LAR=2.2$ . The effect is present more outboard, at 94%, in the case of attached flow. For totally detached flow it can be conjectured that the reduction of the loading starts at a value of  $LAR$ , which corresponds to the value of  $s$  according to Eq. (28). For radial stations outboard of  $s$  an interpolation in two variables is carried out. The two variables are  $LAR$  and proportion of chord ( $f$ ) that is separated. The  $LAR$  value corresponding to a certain value of  $f$  is gleaned from the Ronsten [14] - [16] and Simms [20] reports, where the attached flow is affected within a  $LAR$  value = 1 and for detached flow  $LAR = s^2/A$  respectively. A straight line relationship is assumed as seen in Fig. 29.

To arrive at an algorithm for an arbitrary level of stall the steps 1 – 6 above can be used in a modified form as follows. Input to the algorithm is  $C_{D90}$ ,  $C_n$ ,  $\alpha$  and the angle of attack for zero lift ( $\alpha_0$ ).

**ALGORITHM:**

1. Find  $s$  according to Eq. (28). Apply iteration, according to Fig. 10, if the chord is not constant.
2. Create the corresponding value of  $LAR$ , i.e.  $LAR_0 = s^2/A$ .
3. Calculate a value of  $f$  accordingly (See Appendix A):

$$\begin{array}{llll}
 aa = & 0.149398407 & ba = & -0.06195778 & ca = & 0.025315784 & da = & -0.001529882 \\
 ab = & -0.309142373 & bb = & 0.349459195 & cb = & -0.108291675 & db = & 0.007827487 \\
 ac = & -0.023715832 & bc = & -0.164404434 & cc = & 0.069789982 & dc = & -0.00568632 \\
 ad = & 0.086426002 & bd = & -0.013828726 & cd = & -0.005941372 & dd = & 0.00070752
 \end{array}
 \tag{63}$$

$$\begin{aligned}
 A &= aa + ab \cdot CD90 + ac \cdot CD90^2 + ad \cdot CD90^3 \\
 B &= ba + bb \cdot CD90 + bc \cdot CD90^2 + bd \cdot CD90^3 \\
 C &= ca + cb \cdot CD90 + cc \cdot CD90^2 + cd \cdot CD90^3 \\
 D &= da + db \cdot CD90 + dc \cdot CD90^2 + dd \cdot CD90^3
 \end{aligned}
 \tag{64}$$

After insertion of  $aa$ ,  $ab$  etc in the expressions for  $A$ ,  $B$ ,  $C$  and  $D$ ,  $f$  is obtained through:

$$x \equiv \frac{C_n}{\sin(\alpha - \alpha_0)} \quad \text{(definition)} \tag{65}$$

$$f \approx Ax + Bx^2 + Cx^3 + Dx^4 \tag{66}$$

4. Calculate the  $LAR$  value where reduction starts according to the straight line assumption, i.e.  $LAR^* = LAR_0 + (LAR_1 - LAR_0) \cdot f$  where  $LAR_1 = 1$  (67)

5. Calculate the station  $LAR$  value at input value of  $y$ :  $LAR = y^2 / A$  (68)

6. If  $LAR < LAR^*$  continue to the next step, else  $g = 1$  and the calculation is finished.

7. Calculate the factor  $g = \left\{ 1 - \left( 1 - \frac{LAR}{LAR^*} \right)^e \right\}^{1/e}$  where  $e = 2.5$  (69)

8. for all angle of attack values in the 2D aero table do:  $C_{L,3D} = g C_{L,2D}$ ;  $C_{m,3D} = g C_{m,2D}$ ;  $C_{D,3D} = C_{D,2D}$  (70)

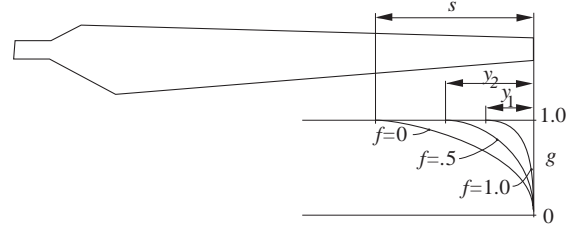


Figure 30

It is finally pointed out that these preparatory calculations are referred to the circumstances before a reduction, using the factor  $g$ , has been carried out. Thus, no iteration is necessary.

### 3.3 THE HIMMELSKAMP EFFECT

As in the case of the tip effects the root area of the blade is subject to radial gradient effects. The Himmelskamp effect is superimposed on the radial gradient effect. Moreover, there is a transition effect where the Himmelskamp part depends on RPM. These three phenomena interact in a fashion which is concealed to the observer because of inherent difficulties to separate the three and because of lack of sufficient amounts of measured data. As will be shown, the gradient effect will not be applied in the same manner because it is taken care of by the transition effect, as demonstrated in the following text.

The boundary layer on a rotating blade is subject to centrifugal forces, which transport parts of the layer, which can be called an “air lump”, toward a larger radius. If the air lump were to stay on the same chordwise position it would be traveling faster in the tangential direction. Such a situation would be equivalent with an acceleration in the tangential direction. This is opposed by an opposite mass inertia force trying to pull the air lump toward the trailing edge. The latter force, which is equal to the Coriolis force, works the same way as a favorable pressure gradient. As a result the air lump can withstand a higher adverse pressure gradient on a rotating blade than on a fixed wing. The consequence is that separation, for a given angle of attack and Reynolds number, occurs at a position aft of that which would have been the case on a fixed wing. This phenomenon was first recorded in 1940 by German researcher Himmelskamp. He performed wind tunnel tests on instrumented propellers, allowing the evaluation of pressure distributions, and he presented  $C_L$  values in excess of 3.0 for radial stations near the hub. Although Himmelskamp found the consequences of this particular aerodynamic phenomenon he did not present a theory explaining his findings. His doctoral thesis from 1945 includes descriptions of his measurements, see Ref. [5].

#### 3.3.1 CL Modification

Qualitative explanations of the Himmelskamp effect were presented in the late 80s. Notably Dutch researcher H. Snel et al derived a simplified set of Navier – Stokes equations valid for a quasi-two-dimensional boundary layers, where centrifugal and consequential Coriolis effects were accounted for. It appears, in his final expression for  $C_L$ , that the crucial factor, driving the Himmelskamp effect, is chord divided by radius ( $c/r$ ). This method was expedient to use as an add-on to existing computer code. His final equation for lift is now being used with modifications flavored by each wind turbine engineer trying to fit measured data to the Snel lift equation.

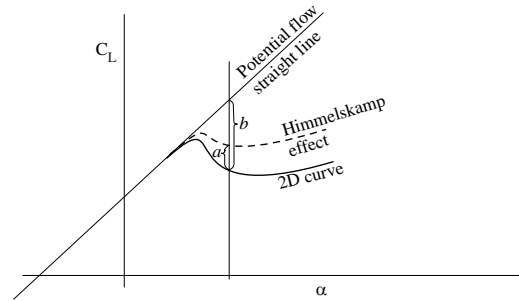


Figure 31

The Snel approach is applied also in this report with some additional thoughts for the corresponding drag and moment effects. With reference to Fig. 31 the Snel additional lift can be expressed as  $a$ . It constitutes a fraction of the measure  $b$ . The ratio therefore is a number between 0 and 1. Ref.[6] gives the following form for the ratio

$$k = \frac{a}{b} = 3 \left( \frac{c}{r} \right)^2 \quad (71)$$

The authors of Ref. [6], however, caution against this quantity formally being in excess of 1.0. A remedy is to replace it with the following expression.

$$k = \frac{a}{b} = \tanh \left\{ 3 \left( \frac{c}{r} \right)^2 \right\} \quad (72)$$

This function, for small values of the argument  $c/r$ , is identical to its argument, while it cannot exceed the value of 1.0 for larger values of the argument.

The typical application of this formula is to replace the coefficient 3 and the exponent 2 with parameter values, which can be adapted to measurements. In summary the  $C_L$  adjustment, caused by the Himmelskamp effect, can be written

$$C_L = C_{L,2D} + \tanh \left\{ d \left( \frac{c}{r} \right)^e \right\} (C_{L,invicid} - C_{L,2D}) \equiv C_{L,2D} + \delta C_L \quad (73)$$

For complete expression see 3.3.4

where the last member defines the quantity  $\delta C_L$  (also denoted  $a$ , see Eq. (72)). Before emerging data from measurement will become available the default values should be  $d = 3$  and  $e = 2$ .

One very important consideration is to determine at what angle of attack to terminate the Himmelskamp effect in order to prepare for a "soft landing" on the thin plate curve. Although there is no firm evidence how to proceed in this matter the following procedure will be used.

The unrestricted application of the Himmelskamp effect, according to Eq. (73), would lead to unrealistic values for very high and very low angles of attack. Therefore an assumption, concerning the probable behavior at these high angles, must be made. It is assumed that the Himmelskamp effect is reduced to a low level above say 45 degrees. But, this should also be true on the negative side. Moreover at round the linear part at 180 degrees the full Himmelskamp effect should be present. This reasoning leads to the conclusion that the Himmelskamp effect should be subdued between approximately  $-140$  to  $-40$  degrees

and between 45 and 140 degrees angle of attack. For practical application these thoughts can be listed as a sequence of steps with reference to Fig. 32.

Step 1: The basic assumption is that the original curve is somehow available in the complete interval from  $-180$  to  $+180$  degrees. This curve may, or may not, be representative for 2D circumstances. But, it is important that the curve does not represent rotational data. The curve may, however, have been produced from an experiment with an aspect ratio of the wing which is finite, such as was frequently the case in the early NACA tests, where  $AR=6$  was typically applied.

Step 2: The linear parts of the CL curve are identified and their linear approximations are established (linear curve fits).

Step 3: The Snel equation is applied to yield interpolated curves, not only at positive CLs, but also at all four positions where the Himmelskamp physics apply, see A, B, C and D. The CL curves obtained in this way will be called "rawSnelCL".

Step 4: If all interpolated curves from step 3 were to be extrapolated there would not be one coherent curve. Nor would there be finite values as the angles tend to infinity. A realistic improvement is called for.

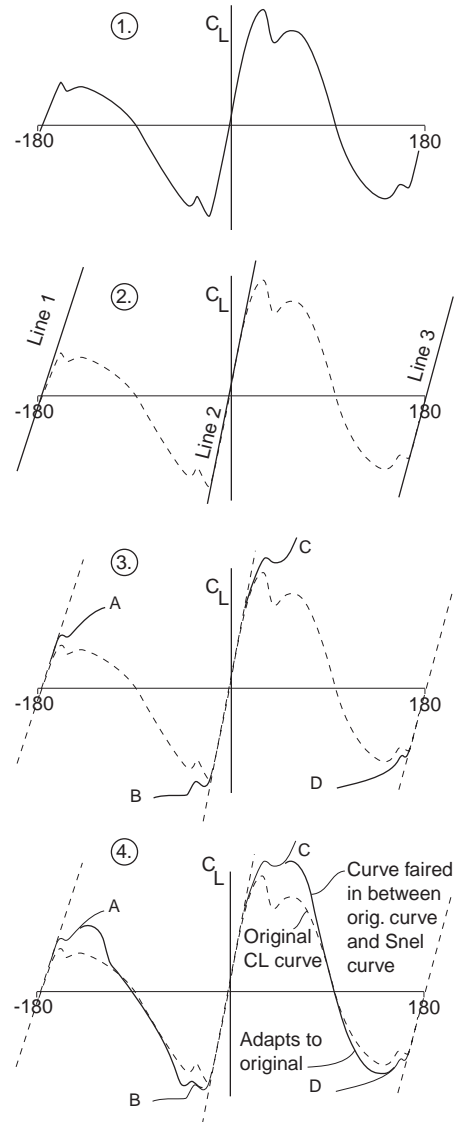


Figure 32

The improvement consists of letting the interpolated curves at A, B, C and D “snuggle up” toward the basic curve.

The four steps of thought described above can be captured in equations, which are adaptable to easy computer programming. Since the ideas are simple and the algorithms become complicated, because of several switches between angular regions, the author refrains from presenting a complete algorithm. The essentials will, however, be presented here. The program code will have to be accepted also as documentation in this respect.

First the equations for the three lines (step 2) are established. This should be done such that they coincide as much as possible with the pre-existing basic curve. Then the Snel equation, Eq. (73), is applied to the regions indicated by A, B, C and D, where A extends to  $-90^\circ$ , B from  $-90^\circ$ , C up to  $+90^\circ$  and D from  $+90^\circ$ .

As indicated previously approaching  $90^\circ$  with this technique yields unphysical values. Therefore step 4 is applied by means of an interpolation function  $h$  whose characteristics are seen in Fig. 33, part 6. It is to be applied to an interpolated function from the A, B, C or D curve to the basic CL curve. This function must be created somewhat heuristically. It could have been made equal to the  $f$  function according to Eq. 44. But, it was felt that some freedom of shaping the details of the complicated  $h$  curve calls for an independent approach. Testing of ideas in a spread sheet program gave support to apply the following method.

First it is noted that a basic “soft ramp” function is needed (any one of the flanks of the  $h$  curve). The following expression is chosen.

$$y = \frac{1}{2} - \frac{1}{\pi} \arctan\{k \cdot \alpha\} \quad (74)$$

The corresponding graph is seen in Fig. 33, part 1. The point P is at the value of one half. It will be referred to as the mid-point. The factor  $k$  determines how steep the transition from level 0 to 1.0 is. The mid-point can be sideways shifted to any location  $\alpha^*$  by a slight modification of the expression accordingly.

$$y = \frac{1}{2} - \frac{1}{\pi} \arctan\{k \cdot (\alpha - \alpha^*)\} \quad (75)$$

The curve, according to part 1 of the figure, can be turned upside down by changing the sign before the arctan function term. Thus all combinations of possibilities seen in 2, 3, 4, and 5 are controlled using  $k$ ,  $\alpha^*$  and switching sign before the arctan function.

Changing notation ( $y \rightarrow h$ ), the desired function is now obtained by combining the four different curves.

$$h = h_1 + h_2 \cdot h_3 + h_4 \quad (76)$$

Then the following expression is used for interpolation.

$$finalCL = h \cdot rawSnelCL + (1-h)originalCL \quad (77)$$

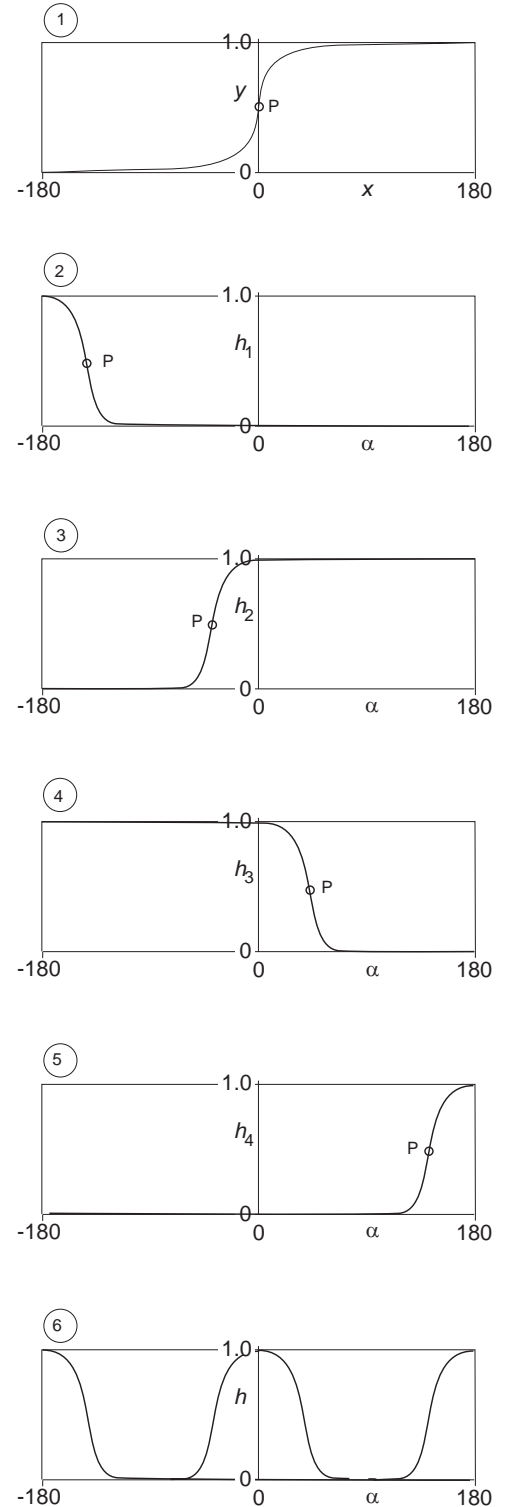


Figure 33

where the “*rawSnelCL*” value is obtained from Eq. (73). A numerical example, that the author tested and found to give reasonable results, had the control parameters that are seen in the following expressions.

$$h_1 = \frac{1}{2} - \arctan\{6(\alpha + 180 - 30)\} \quad (78)$$

$$h_2 = \frac{1}{2} + \arctan\{6(\alpha + 30)\} \quad (79)$$

$$h_3 = \frac{1}{2} - \arctan\{6(\alpha - 45)\} \quad (80)$$

$$h_4 = \frac{1}{2} + \arctan\{6(\alpha - 180 + 30)\} \quad (81)$$

### 3.3.2 CD Modification

#### 3.3.2.1 Background

Along with the lift increase near the hub, which is quite conspicuous,  $CL_{max}$  values of 2.5 can easily be obtained, there is also an effect on drag. The typical behavior of Himmelskamp drag, as a result of calculation, is lower than 2D drag whereas some FFA measurements, see Ref. [7], shows a mixed or opposite trend. The reason for increased drag, in relation to the 2D corresponding drag at same  $\alpha$ , could be that the blade rotation maintains a lower pressure over the rear flank of the suction side of the airfoil where the flow is separated. In fact, where the pressure is almost constant, in the separated part of the surface flow for the 2D case, the 3D rotating situation shows a pressure gradient pointing toward the trailing edge, see Fig. 34. This pressure gradient opposes the Coriolis force thus maintaining a balance, which permits the separated flow to stay over the rear part of the surface while being transported toward the tip by centrifugal forces. See Ref. [5] for a fuller explanation. The situation in the separated region is probably more stable than that in 2D because of the orderly swirl that has been observed to take place there. These effects suggest the separate treatment of the separated rear flank flow.

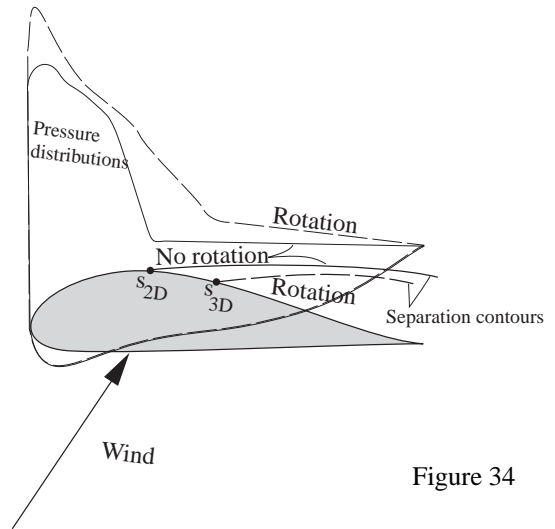


Figure 34

In order to model this effect the low pressure, in the separated region, will be used to generate a surface force which must be perfectly perpendicular to the surface if, as a suitable approximation, friction forces between the air and the surface are ignored in this region, see Fig.35. But, the method will not model the rear flank pressure directly. Instead the following approach will be taken.

#### 3.3.2.2 Lift Implications

From Eq.(73) an increase in  $C_L$ , in relation to the non-rotating case, in physical reality is assumed to emanate from two effects. *Firstly* the chordwise location of the separation line is shifted further aft (stall delay). This gives a higher level of circulation, which translates into higher lift and lower drag. *Secondly*, the rear flank separated area will experience a lower pressure resulting in a component in drag direction (with a corresponding component in lift direction). However, both incremental lift contributions from the Himmelskamp effect are calculated collectively as one quantity, the rotational additional lift, simply from Eq. (73).

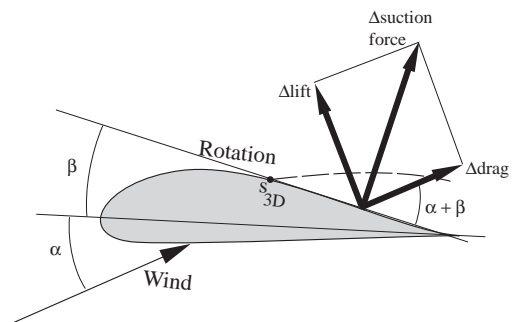


Figure 35

### 3.3.2.3 Drag Implications

The drag implications will be clarified as follows. Two situations are compared to each other. One is the non-rotating case. The other is the rotating case. All comparisons made below will refer to the rotating case in *relation* to the non-rotating case unless otherwise stated. This is also true when the word *differential* is used.

The method is based on dividing the rotational additional lift between the two effects described above. Thus, one portion will be ascribed to increased circulation. The other likewise to the rear flank increased suction. At the present stage of knowledge there is no firm basis for such a distribution. The technique will therefore have to rely on a parameter  $p$ , in an interval  $0 < p < 1$ .  $p$  can be seen as a model parameter, with the hope that present and future investigations will furnish the data necessary to assign a value, or functional relationship, to  $p$ . How  $p$  is to be used is dealt with below.

#### Vortical drag:

The rotating case has a separation point located further aft. This allows a higher level of circulation, hence more lift. Because of the thinner wake, drag should be reduced. Both of these effects can be ascribed to the increased circulation, giving rise to a lift increase that can be called  $\delta C_L$  (not to be confused with  $\Delta C_L$ ). The parameter  $p$ , a number between 0 and 1, mentioned above is used such that it is the proportion that is circulatory.  $(1-p)$  must be the rest, i.e. the rear flank lift, which is thought to be vortical. In Fig. 35 it is called  $\Delta$ lift. To emphasize the coefficient aspect we will use the notation  $\Delta C_{L,vort}$  instead.

$$\Delta C_{L,vort} = (1-p)\delta C_L \quad (82)$$

In the separated region rotating, the pressure is lower thus giving rise to a local differential force that acts in a direction perpendicular to the surface. I.e. such is the case if friction forces are ignored. Since, in separated flow, pressure effects dominate the force buildup totally, such an omission is acceptable.

When the additional force is projected perpendicular to the flow and parallel with it the incremental lift and drag components respectively are generated. Since the situations in focus generally occur at high angles of attack and furthermore the rear upper flank angle of the airfoil surface must be added to the angle of attack, i.e.  $\alpha + \beta$ , the angle used in the vector sub-component generation is quite large compared to normal angles of attack. This gives considerable contributions to drag.

It is emphasized that the method is incremental, building on presumed known aerodynamic behavior at circumstances, which can be described as non-rotating and two-dimensional. Thus the incremental effects are = (those 3D) – (those 2D). Fig. 35 shows the projection of the incremental rear surface force. The angle of attack and airfoil shape sketched are probably realistic under heavily stalled circumstances. The result is that the vortical lift and drag contributions are of same order of magnitude even same size sometimes.

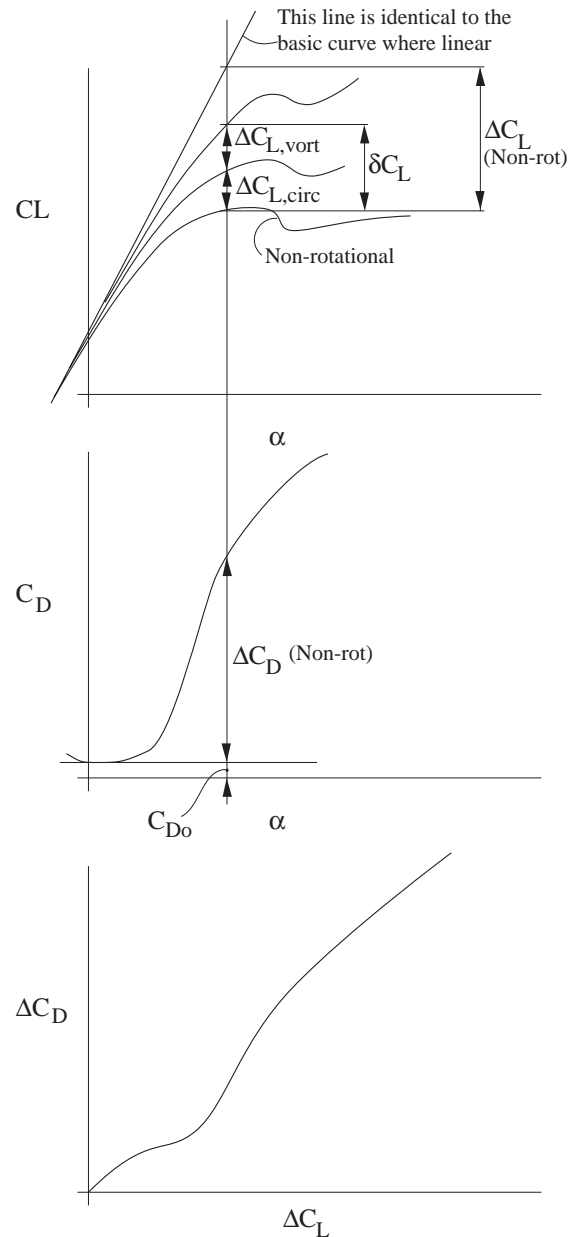


Figure 36



$$\Delta C_{D,vort} = \Delta C_{L,vort} \tan(\alpha + \beta) \quad (83)$$

The angle  $\beta$  is obtained from statistics as described in the algorithm further down the text.

#### Attached flow lift and drag:

There is a need to obtain both lift and drag pertaining solely to the attached flow preceding the separated region. The complete lift or drag thus is the sum of the attached flow coefficient and the coefficient that is generated in the separated region of the airfoil. First we need to establish the Himmelskamp additional attached lift as follows.

$$\Delta C_{L,circ} = p \cdot \delta C_L \quad (84)$$

The loss in  $C_L$ , see  $\Delta C_L$  in Fig. 36a, can be seen as a deficit in relation to the imaginary continuation of the "potential flow" lift curve depicted as a straight line in the  $C_L$  vs  $\alpha$  diagram. The deficit is the result of separation leading to a lesser circulation.

The widening separation region, as  $\alpha$  increases, is also associated with an increasing loss of momentum of the flow, thus drag. By allowing the potential flow line to be integral with the lift curve, for low values of  $\alpha$ , some loss of circulation has already been ignored. The reason is that the boundary layer, how ever thin, generates both drag and loss of circulation. The very small effects associated with the substall angles of attack are filtered away by using the technique of making the line perfectly identical with the  $C_L$  curve where it is straight. This technique also reflects in the  $C_D$  diagram, Fig. 36b, such that  $C_{D0}$  is ignored.

The third diagram in Fig. 36 is a plot of  $\Delta C_D$  vs  $\Delta C_L$  which can be thought of as one separation effect vs another separation effect. The audacious assumption is made that this curve will be valid even after Himmelskamp manipulation of the  $C_L$  curve! This allows calculation of  $C_D$  – not including the rear flank extra drag as discussed above. First the new  $C_L$  curve is established with tip effects and Himmelskamp effects. Then the already existing curve from Fig. 36c is used together with the new  $C_L$  curve to create a new  $C_D$  vs  $\alpha$  diagram.

Difficulties of a practical nature will arise. E.g. the 2D data, as of Fig. 36, may not extend all the way to where the new  $C_L$  curve reaches. The remedy is extrapolation of the curve in 36c. Investigation of the nature of this curve has been carried out by this author previously and for several different airfoils the relationship appeared to be essentially linear. The slope was found to be = 0.13 apart from the bulge seen in the figure. The bulge only appears for symmetrical and thick airfoils, see Ref. [6], p. 20.

### 3.3.3 Cm Modification

In analogy with what is proposed for lift and drag there will be an effect in the moment coefficient as well. Only one single experimental data source of information has been available to investigate the matter, see Ref. [14]. From it Fig. 31 was extracted. It represents pressure coefficient ( $C_p$ ) distributions in standard interpretation format. It demonstrates the significance of the parameter  $c/r$ . The value  $c/r = 0.377$  is associated with more than doubling the area within the  $C_p$  loop, when the non-rotational data (crosses) are compared with rotational ditto (circles). The distance from the 25% chord point to the center of gravity (CG) of the  $C_p$  area is the moment arm, which, multiplied by the area within the  $C_p$  loop gives the moment coefficient ( $C_m$ ). Visual inspection of the left part of Fig. 31 immediately reveals that the CG of the area, enclosed by the pressure curve, is at a more forward position for the rotational case, because the loop is more of a pure triangle compared to the non-rotational loop.

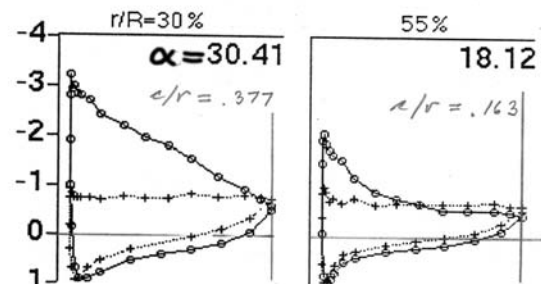


Figure 31



Several simplifying assumptions were made in order to prepare for a simple comparative analysis. By assuming that the airfoil is a non-cambered flat thin plate the normal and the moment coefficients can be calculated, for all four distributions. This was done in the hope that incremental differences (although not absolute numbers) could be derived from such an approach.

The data were utilized in the following manner.

1. Moments ( $Cm$ ) and normal coefficients ( $C_N$ ) were evaluated.
2. The moment arms (to the 25% chord point) were calculated from  $a = Cm/ C_N$ .
3. The difference between rotating and non-rotating  $C_N$  values were calculated and were called  $\Delta C_N$ , one for each  $\alpha$ .
4. The difference between rotating and non-rotating moment arm values were calculated and were called  $\Delta a$ , one for each  $\alpha$ .
5. The thus resulting two points  $(\Delta C_N, \Delta a)_{\alpha=30.41} = (1.177, 0.011)$  and  $(\Delta C_N, \Delta a)_{\alpha=18.12} = (0.227, 0.058)$  were plotted in a diagram with  $\Delta C_N$  on the abscissa and  $\Delta a$  on the ordinate.
6. Analyzing the two points in the diagram it seemed unlikely that the connecting relationship between the two points could be a straight line. The trend from the two points is that  $\Delta a$  decreases with increasing values of  $\Delta C_N$ . But there seems to be no reason why the line should cross over the x axis and become negative. Negative values would lead to the  $Cp$  CG moving up forward of the 25% point and that should be avoided. So, it was assumed that the curve connecting the two points should be an asymptote to the x axis (in fact the  $\Delta C_N$  axis).
7. The two points and the assumption from point 6 lead to the curve fit expression see Eq. (87).
8. Then Ref. [15] was used for an extended number of check points available in Figs. 8a and 8c in that report. The technical difference was that the angle of attack had been calculated using different methods. It turned out that the correlation between the two sets of information was reasonable considering the expected level of approximation. The unifying technique was to interpolate the sets of constants seen in Eq. (87) from the two data sets. The final numerical values of the described elaboration are seen in Eq. (87).

The conclusions can be summarized in an algorithm as follows.

*Algorithm:*

1. Calculate, if need be,  $C_{No}$  from the angle of attack ( $\alpha$ ),  $C_{Lo}$  and  $C_{Do}$  where the subscript “o” signifies non-rotational conditions.
2. Calculate the moment arm using

$$a_o = -C_{mo}/C_{No} \quad (85)$$

where  $a_o$  is counted from the 25% chord point, positive toward the trailing edge of the profile.

3. Calculate  $C_L$  and  $C_D$  using the method adapted to the Himmelskamp (rotational) effect, for the given value of  $\alpha$ .
4. Calculate the normal coefficient  $C_N$  from  $\alpha$ ,  $C_L$  and  $C_D$ .

5. Create the difference  $\Delta C_N = C_N - C_{No}$  (86)

6. Calculate the negative increment in moment arm using:  $\Delta a = -\frac{1.2}{1 + 8\Delta C_N^2}$  (87)

7. Calculate the final value of the moment coefficient accordingly:  
 $C_m = C_N \cdot (a_o + \Delta a)$  (88)

### 3.3.4 Variability with RPM

At very low RPMs there is no Himmelskamp effect. The theory of Ref. [6] does not deal with RPM. It simply assumes it is not zero. At this point in time there is no exact knowledge about the RPM transition behavior of the Himmelskamp effect. An approximation from Ref. [21] is used accordingly.

$\delta C_L$  (See Eq. (73) is replaced by  $\delta C_L \cdot \lambda^2 / (1 + \lambda^2)$  (89)

where  $\lambda$  is to be interpreted as the *local* speed ratio with due respect to any axial induction.

### 3.3.5 Summary of Measures taken to Account for the Himmelskamp Effect

A compact description of the intricacies dealt with in the previous section follows.

1. The Himmelskamp effect is calculated for  $\delta C_L$  using Eq. (73) and Eq. (89)
2. The parameter  $p$ , which is a model parameter number between 0 and 1.0, is applied to get

$$\Delta C_{L,circ} = p \cdot \delta C_L \quad (90)$$

$$\Delta C_{L,vort} = (1 - p) \cdot \delta C_L \quad (91)$$

3. The vortical drag part is obtained using the angle  $\beta$ , which is obtained from basic geometric characteristics accordingly:

Input:  $t/c$  = Profile relative thickness  
 $h/c$  = Profile maximum camber

where  $h$  is the height from the reference line to the mean line maximum. An equation for the rear flank angle  $\beta$ , see Fig. 35, was found from analysis of a few typical airfoils:

$$\beta^\circ = 57.3 * (1.04 \frac{t}{c} + 2 \frac{h}{c}) \quad (92)$$

$$\Delta C_{D,vort} = \Delta C_{L,vort} \cdot \tan(\alpha + \beta) \quad (93)$$

If more accurate information is available about the rear flank angle  $\beta$ , that information should be used in place of the simplified formula according to Eq. (92).

Finally the basic drag, even called “attached flow drag” above, is obtained from reading off the data from the diagram in Fig. 36c, which will have to be constructed first.

To calculate  $C_m$  the algorithm given in section 3.3.3 is followed.

#### **4. TOPICS FOR FUTURE INVESTIGATION**

The ideas presented in this document are based on a combination of observation and theory. The observations mainly refer to measured data with a few exceptions for CFD calculations, which show the same trends. But, there is a long chain of linked dependence from basic two-dimensional aerodynamic tables to the calculated performance of a propeller or a wind turbine rotor. It is therefore necessary to get access to future measurements and to utilize the data from the measurements in order to tune the model parameters of the many methods presented in the document. Moreover, it will most likely be necessary even to change the algorithms whenever conclusive studies obviate such a need. The generation of the overall method described here is to be seen as a beginning of a process, which should be continuously refined. This will require, first of all, access to high quality experimental data. But, the future might even gradually allow increasing dependence on CFD methods, whose results can be treated as experimental data.



## 5. REFERENCES

- [1] Aerodynamic Characteristics of NACA 0012 Airfoil Section at Angles of Attack from 0° to 180°. Cris C. Critzos et al. NACA Tech. Note 3361
- [2] FLUID DYNAMIC LIFT  
S. F. Hoerner and H. V. Borst  
Published by Mrs Liselot Hoerner, 1975  
Especially Chapt. 4 and Eqs. (17) and (18)
- [3] FLUID DYNAMIC DRAG  
Sieghard F. Hoerner  
1965 issue  
Published by Mrs Liselot Hoerner
- [4] Drag Coefficient Distribution on a Wing at 90 Degrees to the Wind  
February 1996  
Bjorn Montgomerie  
Netherlands Energy Research Foundation ECN  
Rep: ECN-C—95-061
- [5] Profile Investigations on a Rotating Airscrew  
Himmelskamp  
PhD Dissertation, Göttingen 1945  
Also: Profiluntersuchungen an einem umlaufenden Propeller  
Mitteilungen aus dem Max-Planck-Institut für Strömungsforschung, Nr.2 – Göttingen 1950
- [6] Sectional Prediction of Lift Coefficients on Rotating Wind Turbine Blades in Stall  
H. Snel, R. Houwink, J. Bosschers  
Netherlands Energy Research Foundation  
Rep: ECN-C—93-052
- [7] Horizontal Axis Wind Turbine Post Stall Airfoil Characteristics Synthesization  
James L. Tangler and Cyrus Ostowari  
Paper of unknown origin except that the work performed was under contract no. DE-AC04-760p03533 for the US Dep. Of Energy. – Approximately 1984
- [8] Post Stall Studies of Untwisted Varying Aspect Ratio Blades with a NACA 4415 Airfoil Section – Part I  
C. Ostowari and D. Naik, Aerospace Engineering Dep., Texas A&M University, College Station, Texas 77843, USA  
Publisher: Wind Engineering, Vol. 8, No.3, 1984
- [9] Post Stall Studies of Untwisted Varying Aspect Ratio Blades with a NACA 4415 Airfoil Section - Part II  
C. Ostowari and D. Naik, Aerospace Engineering Dep., Texas A&M University, College Station, Texas 77843, USA  
Publisher: Wind Engineering, Vol. 9, No.3, 1985
- [10] Quasi Steady Aerodynamic Coefficients at a Large Range of Angles of Attack  
Arno Brand and Bjorn Montgomerie  
The Netherlands Energy Research Foundation (ECN)  
Rep. ECN – C -- 95 - 059

- [11] Airfoil Characteristics for Wind Turbines  
Christian Bak et al  
Risø National Laboratory, Roskilde, Denmark  
Rep. Risø-R-1065(EN)
- [12] Chinese report from CAARDC about 1985, written in the Chinese language, with several profiles tested in wind tunnel in an angle of attack range from 0 to 180 degrees.
- [13] “Fixed Pitch Rotor Performance of Large Horizontal Axis Wind Turbines”  
L. A. Viterna and R. D. Corrigan  
Proceedings, Workshop on Large Horizontal Axis Wind Turbines, NASA CP-2230, DOE Publication CONF-810752, Cleveland Ohio, NASA Lewis Center, pp. 69 – 85.  
Also the following textbook, p. 289, explains the VC equations in a direct and compact form:  
“Wind Turbine Technology”, David A. Spera, Editor - ASME Press, Lib. Of Congress Cat. Nr: 94-11137
- [14] “Static Pressure Measurements on a Rotating and Non-rotating 2.375 m Wind Turbine Blade – Comparison with 2D Calculations”  
Göran Ronsten, the Aeronautical Research Institute of Sweden (FFA)  
Rep. nr: FFA TN 1991-36
- [15] “Aerodynamic Section Characteristics of a Rotating and Non-rotating 2.375m Wind Turbine Blade”  
Anders Björck, Göran Ronsten and Björn Montgomerie, the Aeronautical Research Institute of Sweden (FFA)  
Rep. nr: FFA TN 1995-03
- [16] “Geometry and Installation in Wind Tunnels of a Stork 5.0 WPX Wind Turbine Blade Equipped with Pressure Taps”  
Göran Ronsten, the Aeronautical Research Institute of Sweden (FFA)  
Rep. nr: FFAP-A 1006 (1994)
- [17] “Measured Airfoil Characteristics of Three Blade Segments on a 19m HAWT Rotor”  
Contribution to the 3<sup>rd</sup> IEA Joint Action Meeting on Wind Turbine Aerodynamics  
at the Hartwell Lab., UK, Nov. 1989  
Available in the Proceedings – edited by K. F. McAnulty, June 1990  
Authors: Helge A. Madsen, Flemming Rasmussen  
Test Station for Wind Turbines, Risoe National Laboratory, Roskilde, Denmark
- [18] “Evaluation of 3D Effects from 3D CFD Computations”  
Contribution to the 14th IEA Joint Action Meeting on Wind Turbine Aerodynamics at NREL, Boulder Co., December 2000  
Available in the Proceedings – edited by K. F. McAnulty, June 1990  
Author: Niels N. Sørensen  
Wind Energy and Atmospheric Physics Department, Risoe National Laboratory, Roskilde, Denmark
- [19] “Inviscid Stall Model”  
Gustave P. Corten, The Energy Research Foundation (ECN) the Netherlands.  
Contribution to IEA Joint Action on Aerodynamics of Wind Turbines, 14<sup>th</sup> Symposium, Boulder Col., USA, organized by NREL, December 2000
- [20] “Characterization and Comparison of Baseline Aerodynamic Performance of Optimally Twisted vs Non-Twisted HAWT Blades”  
Dave Simms et al, NREL, ASME 1996
- [21] Private communication with Koert Lindenburch of ECN, Netherlands, who gives the following explanation in a letter:  
The transition is a factor  $\lambda^2/(1 + \lambda^2)$ . This factor is multiplied by the "3.1 (c/r)<sup>2</sup>" correction term in the method of Snel et. al. <See Ref. [6] above> Here  $\lambda$  is the *local* speed ratio! The basis for this factor is the

fact that the driving pressures for the effects of rotation are proportional to  $(\omega r)^2$  while the dynamic pressure of the relative flow on the airfoil is  $(\omega r)^2 + (U_{\text{wind}} - U_i)^2$ . Here 'r' is the local radius and 'U<sub>i</sub>' is the induced velocity. The ratio between the driving pressures and the dynamic pressure can be reduced to  $\lambda^2 / (1 + \lambda^2)$ .

[22] XFOIL is a computer program freely available from the site of the creator(s). It uses the boundary layer integral technique and potential flow pressure distribution in an iterative hard-coupled way. The free version is being maintained by:

Mark Drela, MIT Aero & Astro and Harold Youngren, Aircraft, Inc.

At the time of writing it could be accessed at: <http://raphael.mit.edu/xfoil/>





# Appendix A

## NORMAL COEFFICIENT AS A FUNCTION OF ANGLE OF ATTACK AND SEPARATION LOCATION

### 1. BACKGROUND

The need for aerodynamic relations valid for deep stall conditions lead to this study. A fundamental idea is that the point in a  $C_n(\alpha)$  plane will always soar between two curves. Those curves are that for perfectly attached flow and that for perfectly separated flow. They can be thought of as "fences" for the freedom of a  $C_n(\alpha)$  point.

For the curve for attached flow, sometimes referred to as the potential flow curve, the separation parameter  $f = 1$ . The  $f$  parameter signifies the number of chord lengths that the flow is attached (length to separation relative to the chord), in this case all the way to the trailing edge. Correspondingly at fully separated flow  $f$  has a value of zero.

The text below deals with the task to find an empirical relationship between the normal coefficient ( $C_n$ ),  $\alpha$  and  $f$ .

### 2. EQUATIONS

Leishman and Beddoes, Ref. 1, present a relation, usually referred to as the Kirchoff law, that reads as follows – using  $\alpha$  to denote the angle of attack as usual.

$$C_n = 2\pi \left( \frac{1 + \sqrt{f}}{2} \right)^2 \alpha \quad (1)$$

Here  $\alpha$  is to be interpreted to mean the angle of attack counted from the zero lift angle of attack.  $C_n$  is the normal coefficient. Hoerner, Ref. 2, p. 4 – 23, presents the following expression for totally stalled airfoil conditions

$$C_{n_{stall}} = (1.8 \text{ to } 2.0) \sin \alpha \quad (2)$$

It should be noted that the number range 1.8 to 2.0 represents the flat plate drag coefficient number at  $\alpha = 90^\circ$ . The notation  $C_{D90}$  will be used to denote this quantity rather than the numerical range – Hoerner fashion.

A comparison between the two related expressions reveals the following similarities and differences.

(1) is valid for a relatively small  $\alpha$  interval from zero up to stall whereas (2), the Hoerner expression, is valid for the complete  $\alpha$  range from 0 to  $\pm 180^\circ$ . (1) has more information of detail since it says something about the degree of stall embodied in the  $f$  parameter.

The Hoerner version is obviously more useful when very high  $\alpha$ :s need to be considered. But, the higher resolution Kirchoff expression is more useful for practical modeling purposes at around normal stall angles.

The following treatment of these two expressions is directed toward fusing them, thereby retaining the good resolution of (1) and bringing the validity to higher  $\alpha$ :s like in (2).

A function  $k$  can be used to be responsible for both the  $C_{D90}$  value and the sensitivity to the location of the separation point  $f$ . Eq. (1) is rewritten using this new function.

$$C_n = 2\pi \left( \frac{1 + \sqrt{f}}{2} \right)^2 \cdot k(f, C_{D90}) \cdot \sin \alpha \quad (3)$$

The requirements on this function must be that it is equal to 1 for unstalled conditions (where  $f = 1$ ). Further it must tend toward  $2C_{D90} / \pi$  for totally stalled situations (where  $f = 0$ ). Then (2) is satisfied. Many forms can be found, which satisfy both requirements. After some numerical experimentation the following expression was selected.

$$k = \left( \frac{2}{\pi} C_{D90} - 1 \right) (1 - f)^2 + 1 \quad (4)$$

The complete expression for  $C_n$  is now obtained from (3) and (4) accordingly.

$$C_n = 2\pi \left( \frac{1 + \sqrt{f}}{2} \right)^2 \cdot \left\{ \left( \frac{2}{\pi} C_{D90} - 1 \right) (1 - f)^2 + 1 \right\} \cdot \sin \alpha \quad (5)$$

It turns out that the more frequent problem calls for  $f$  as a function of  $\alpha$  and  $C_n$ , which is the reversal of Eq. (5). One way of solution could be reached by numerical iteration out of convenience even though a 4th order polynomial root would be possible to solve for analytically. However, a simple curve fit polynomial was found using the "Solve" function in MS Excel. This function could be used to find the inverse of (5).

$$x \equiv \frac{C_n}{\sin \alpha} \quad (\text{definition}) \quad (6)$$

$$f \approx Ax + Bx^2 + Cx^3 + Dx^4 \quad (7)$$

$f$  is an approximation of the inverted function of Eq. (5) judged to be accurate enough. Its value can mathematically be greater than 1.0, which should be prevented in a complete algorithm. Numerical values of the polynomial coefficients were evaluated accordingly.

$$\begin{aligned} A &= aa + ab \cdot CD90 + ac \cdot CD90^2 + ad \cdot CD90^3 \\ B &= ba + bb \cdot CD90 + bc \cdot CD90^2 + bd \cdot CD90^3 \\ C &= ca + cb \cdot CD90 + cc \cdot CD90^2 + cd \cdot CD90^3 \\ D &= da + db \cdot CD90 + dc \cdot CD90^2 + dd \cdot CD90^3 \end{aligned} \quad (8)$$

where

$$\begin{array}{llll} aa = & 0.149398407 & ba = & -0.06195778 & ca = & 0.025315784 & da = & -0.001529882 \\ ab = & -0.309142373 & bb = & 0.349459195 & cb = & -0.108291675 & db = & 0.007827487 \\ (9) & & & & & & & \\ ac = & -0.023715832 & bc = & -0.164404434 & cc = & 0.069789982 & dc = & -0.00568632 \\ ad = & 0.086426002 & bd = & -0.013828726 & cd = & -0.005941372 & dd = & 0.00070752 \end{array}$$

The practical application of this method is therefore:

### 3. ALGORITHM

The figure shows the idea. Follow these steps:

1. Calculate  $A$ ,  $B$ ,  $C$  and  $D$  according to (8).
2. Calculate  $x$  using (6).
3. Calculate  $f$  using (7).



#### **4. COMPARISON**

The figure shows one example of a comparison between  $f$  and its curve fit representation. CD90 was 2.2 for this particular case.

#### **5. REFERENCES**

1. "A Semi-Empirical Model for Dynamic Stall"

by: Leishman and Beddoes

J. of the American Helicopter Soc., July 1989

2. Fluid Dynamic Lift

by: S. Hoerner and H. Borst

Publisher: Mrs. Liselotte Hoerner 1985

<b>Issuing organization</b> FOI – Swedish Defence Research Agency Aeronautics, FFA SE-172 90 Stockholm	<b>Report number, ISRN</b> FOI-R--1305--SE	<b>Report type</b> Scientific report
	<b>Research area code</b> 7. Vehicles	
	<b>Month year</b> June 2004	<b>Project no.</b> E287404
	<b>Customers code</b> STEM	
	<b>Sub area code</b> 76 Wind energy	
<b>Author/s (editor/s)</b> Björn Montgomerie	<b>Project manager</b> Björn Montgomerie	
	<b>Approved by</b> Sven-Erik Thor	
	<b>Sponsoring agency</b> STEM	
	<b>Scientifically and technically responsible</b> Björn Montgomerie	
<b>Report title</b> Methods for Root Effects, Tip Effects and Extending the Angle of Attack Range to $\pm 180$ deg., with Application to Aerodynamics for Blades on Wind Turbines and Propellers		
<b>Abstract</b> <p>For wind turbine and propeller performance calculations aerodynamic data, valid for several radial stations along the blade, are used. For wind turbines the data must be valid for the 360 degree angle of attack range. The reason is that all kinds of abnormal conditions must be analysed especially during the design of the turbine. Frequently aerodynamic data are available from wind tunnel tests where the angle of attack range is from say -5 to +20 degrees. This report describes a method to extend such data to be valid for <math>\pm 180</math> degrees. Previously the extension of the data has been very approximate following the whim of the moment with the analyst.</p> <p>Furthermore, the Himmelskamp effect at the root and tip effects are treated in the complete method.</p>		
<b>Keywords</b> wind, turbine, aerodynamics, Himmelskamp		
<b>Further bibliographic information</b> This report is a draft report whose finishing touches and numerical methods consequences are still missing due to lack of continued funding	<b>Language</b> English	
<b>ISSN</b> 1650-1942	<b>Pages</b> 53 p.	
	<b>Price acc. to pricelist</b>	

<b>Utgivare</b> Totalförsvarets Forskningsinstitut - FOI Flygteknik FFA 172 90 Stockholm	<b>Rapportnummer, ISRN</b> FOI-R--1305--SE	<b>Klassificering</b> Vetenskaplig rapport
	<b>Forskningsområde</b> 7. Farkoster	
	<b>Månad, år</b> Juni 2004	<b>Projektnummer</b> E827404
	<b>Verksamhetsgren</b> 3. Flygteknisk forskning	
	<b>Delområde</b> 76 Vindenergi	
<b>Författare/redaktör</b> Björn Montgomerie	<b>Projektledare</b> Björn Montgomerie	
	<b>Godkänd av</b> Sven-Erik Thor	
	<b>Uppdragsgivare/kundbeteckning</b> STEM	
	<b>Tekniskt och/eller vetenskapligt ansvarig</b> Björn Montgomerie	
<b>Rapportens titel (i översättning)</b> Metoder för roteffekter, spetseffekter och utvidgning av anfallsvinkelområdet till +180 grader, med tillämpning på aerodynamik för vindturbinblad och propellerblad		
<b>Sammanfattning</b> För beräkning av vindturbin- och propellerprestanda behövs aerodynamiska data giltiga för några av bladets tvärsnittprofiler. För speciellt vindturbiner är det nödvändigt, att i samband med simulering, ha tillgång till aerodynamiska data giltiga för anfallsvinklar i hela varvet. Orsaken är att bland andra fall även abnorma extremsituationer måste kunna simuleras. Aerodynamiska data, ofta från vindtunnelprov, finns typiskt tillgängliga för området -5 till +20 grader. I rapportens första del beskrivs en metod för att extrapolera anfallsvinkelområdet till $\pm 180$ grader. Tidigare metodik för extrapolation av anfallsvinkelområdet har varit synnerligen förenklad och olika från gång till gång.  Vidare redogörs för metoder att beräkna tillskott pga Himmelskamp-effekten samt spetseffekter orsakade av radiella tryckgradienter.		
<b>Nyckelord</b> wind, turbine, aerodynamics, Himmelskamp		
<b>Övriga bibliografiska uppgifter</b>	<b>Språk</b> Engelska	
Denna text är ett rapportutkast som saknar en noggrann genomläsning samt en återmatning från numeriska experiment enligt den beskrivna metodiken.		
<b>ISSN</b> 1650-1942	<b>Antal sidor:</b> 53	
<b>Distribution enligt missiv</b>	<b>Pris:</b> Enligt prislista	